UNDERGRADUATE THESIS

**Thesis title:**

Hofstadter butterfly in transistion metal dichalcogenide monolayers

Student: Tran Khoi Nguyen
Supervisor: Dr. Huynh Thanh Duc

Ho Chi Minh City, 2025

NATIONAL UNIVERSITY OF HO CHI MINH CITY
UNIVERSITY OF SCIENCE
FACULTY OF PHYSICS - ENGINEERING PHYSICS

UNDERGRADUATE THESIS

Thesis title:

Hofstadter butterfly in transistion metal dichalcogenide monolayers

_____

Student: Tran Khoi Nguyen
Supervisor: Dr. Huynh Thanh Duc

Ho Chi Minh City, 2025

NATIONAL UNIVERSITY OF HO CHI MINH CITY
UNIVERSITY OF SCIENCE
FACULTY OF PHYSICS - ENGINEERING PHYSICS

Hofstadter butterfly in transistion metal dichalcogenide monolayers

ABSTRACT

Hofstadter's butterfly has been studied experimentally for 50 years. It was first discovered by computer scientist Douglas Hofstadter. This thesis explores the electronic phenomena in material systems, particularly focusing on monolayer transition metal dichacolgenides (TMD). A key focus is on understanding Hofstadter physics. We begin by studying a minimal three-band tight-binding model (TBM) in order to describe the electronic structure of TMD monolayer. We, then, analyze the resulting Hofstadter spectrum under an external magnetic field, reavling the rich fractal stucture. Building on this framework, we further explore related quantum phenomena including Landau levels and quantum Hall effect.

GUARANTEE

ACKNOWLEDGMENTS

TABLE OF CONTENTS

LIST OF FIGURES

LIST OF TABLES

LIST OF ABBREVIATIONS

Abstract

Keywords:

CHAPTER 1

INTRODUCTION

The idea behind Hofstadter's butterfly is that you're looking at how the band structure of electrons moves when you have the magnetic field on one axis and the electrons' energies on the other, and plotted on that diagram, the band forms a fractal structure that looks like a butterfly

CHAPTER 2

THEORY

2.1 Three-band tight binding method without magnetic field
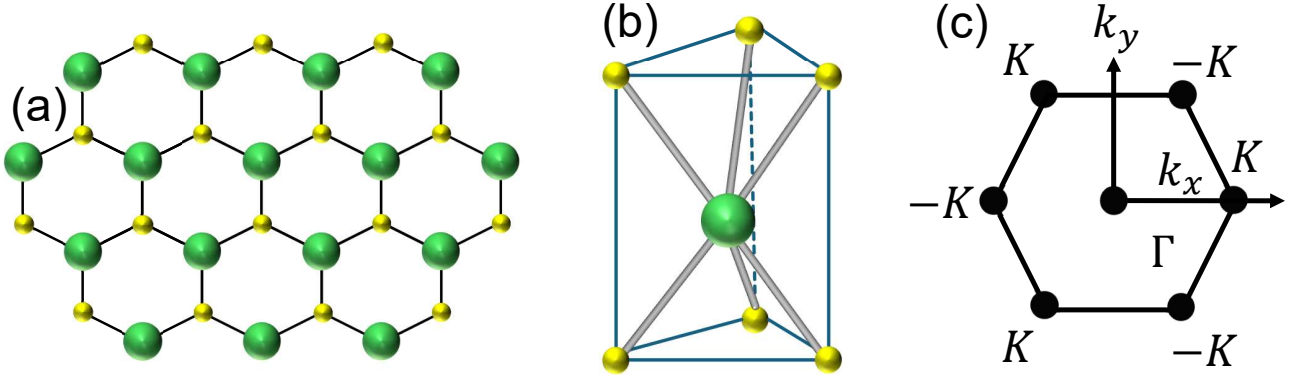
Figure 2.1: Top view of monolayer MX_2. The large sphere is M atom and the small sphere is X.

The time-indepentdent Schrödinger equation for an eletron in the crystal has the form

$$\left[-\frac{\hbar^2\nabla^2}{2m} + U_0(\mathbf{r})\right]\psi_{\lambda,\mathbf{k}}(\mathbf{r}) = \varepsilon_\lambda(\mathbf{k})\psi_{\lambda,\mathbf{k}}(\mathbf{r}), \tag{2.1}$$

where $U_0(\mathbf{r})$ is the periodic lattice potential, $\psi_{\lambda,\mathbf{k}}(\mathbf{r})$ is the Bloch wavefunction of an electron in band λ with wave vector $\mathbf{k}$ and $\varepsilon_\lambda(\mathbf{k})$ is the band structure.

In the tight-binding model (TBM), the single-electron Bloch wavefunction can be expressed in terms of atomic orbitals as follows

$$\psi_{\lambda,\mathbf{k}}(\mathbf{r}) = \sum_{j,i} C_{ji}^\lambda(\mathbf{k})\sum_{\mathbf{R}} e^{i\mathbf{k}\cdot(\mathbf{R}+\mathbf{r_i})}\phi_j(\mathbf{r}-\mathbf{R}-\mathbf{r}_i), \tag{2.2}$$

where $\phi_j(\mathbf{r} - \mathbf{R} - \mathbf{r}_i)$ is the orbital j of an atom i localized on a lattice site $\mathbf{R}$, in which $\mathbf{r}_i$ is the relavetive position of the atom i in the unit cell, and $C_{ji}^\lambda(\mathbf{k})$ are the coeffcents of linear expansion.

The unit cell of TMD involve one transition metal atom M and two chalcogenide atoms X. From the *ab initio* calculations, it is shown that the electron states near the band edges of MX_2 are mainly contributed from the three d orbital of M atom, namely $d_{z^2}, d_{xy}, d_{x^2-y^2}$ [1]. Since only the orbitals of atom M is included, we ignore the sum over the atom $\mathbf{r}_i$ in the unit cell in Eq. (2.2). This model is called the three-band tight binding model. The three orbitals's wave function of M atom are denoted as

$$|\phi_1\rangle = |d_{z^2}\rangle; \quad |\phi_2\rangle = |d_{xy}\rangle; \quad |\phi_3\rangle = |d_{x^2-y^2}\rangle. \tag{2.3}$$

The Bloch wavefunction in this model has the form

$$\psi_{\lambda,\mathbf{k}}(\mathbf{r}) = \sum_{j=1}^{3} C_j^\lambda(\mathbf{k}) \sum_{\mathbf{R}} e^{i\mathbf{k}\cdot\mathbf{R}} \phi_j(\mathbf{r} - \mathbf{R}). \tag{2.4}$$

The coeffcents $C_j^\lambda(\mathbf{k})$ are the solutions of the eigenvalue equation

$$\sum_{jj'} \left[H_{jj'}^{\text{TB}}(\mathbf{k}) - \varepsilon_\lambda(\mathbf{k}) S_{jj'}(\mathbf{k}) \right] C_j^\lambda(\mathbf{k}) = 0, \tag{2.5}$$

where

$$H_{jj'}^{\text{TB}}(\mathbf{k}) = \sum_{\mathbf{R}} e^{i\mathbf{k}\cdot\mathbf{R}} \langle\phi_j(\mathbf{r})| \left[-\frac{\hbar^2\nabla^2}{2m} + U_0(\mathbf{r}) \right] |\phi_{j'}(\mathbf{r} - \mathbf{R})\rangle, \tag{2.6}$$

and

$$S_{jj'}(\mathbf{k}) = \sum_{\mathbf{R}} \langle\phi_j(\mathbf{r})|\phi_{j'}(\mathbf{r} - \mathbf{R})\rangle \approx \delta_{jj'}. \tag{2.7}$$

The three-band tight-binding model often called the nearest-neighbor (NN) since it only includes nearest-neighbor hopping does a decent job matching *ab initio* results near the band edges. However, it starts to break down in other parts of the band structure. This is because the model completely ignores the p orbitals from the X atoms, which stil contributions to the conduction bands at Γ and the valence bands at M. The matrix

elements of the tight-binding (TB) Hamiltonian Eq. (2.6) are

$$
\begin{aligned}
H_{jj'}^{\mathrm{NN}}(\mathbf{k}) = {} & \mathcal{E}_{jj'}(\mathbf{0}) + e^{i\mathbf{k}\cdot\mathbf{R}_1}\mathcal{E}_{jj'}(\mathbf{R}_1) + e^{i\mathbf{k}\cdot\mathbf{R}_2}\mathcal{E}_{jj'}(\mathbf{R}_2) + e^{i\mathbf{k}\cdot\mathbf{R}_3}\mathcal{E}_{jj'}(\mathbf{R}_3) \\
& + e^{i\mathbf{k}\cdot\mathbf{R}_4}\mathcal{E}_{jj'}(\mathbf{R}_4) + e^{i\mathbf{k}\cdot\mathbf{R}_5}\mathcal{E}_{jj'}(\mathbf{R}_5) + e^{i\mathbf{k}\cdot\mathbf{R}_6}\mathcal{E}_{jj'}(\mathbf{R}_6),
\end{aligned}
\tag{2.8}
$$

where

$$
\mathcal{E}_{jj'}(\mathbf{R}) = \left\langle \phi_j(\mathbf{r}) \right| \left[-\frac{\hbar\nabla^2}{2m} + U_0(\mathbf{r}) \right] \left| \phi_{j'}(\mathbf{r} - \mathbf{R}) \right\rangle,
\tag{2.9}
$$

and

$$
\mathbf{R}_1 = (a, 0), \quad \mathbf{R}_2 = \left(\frac{a}{2}, -\frac{a\sqrt{3}}{2} \right), \quad \mathbf{R}_3 = \left(-\frac{a}{2}, -\frac{a\sqrt{3}}{2} \right),
$$
$$
\mathbf{R}_4 = (-a, 0), \quad \mathbf{R}_5 = \left(-\frac{a}{2}, \frac{a\sqrt{3}}{2} \right), \quad \mathbf{R}_3 = \left(\frac{a}{2}, \frac{a\sqrt{3}}{2} \right).
\tag{2.10}
$$

Here, $\mathbf{R}_{1-6}$ are the positions of the nearest neighbors M atoms, see Fig.

g_n	x'	y'	z'	z'^2	$x'y'$	$\frac{1}{2}(x'^2 - y'^2)$
E	x	y	z	z^2	xy	$\frac{1}{2}(x^2 - y^2)$
$C_3(\frac{-2\pi}{3})$	$-\frac{1}{2}x + \frac{\sqrt{3}}{2}y$	$-\frac{\sqrt{3}}{2}x - \frac{1}{2}y$	z	z^2	$-\frac{1}{2}xy + \frac{\sqrt{3}}{4}(x^2 + y^2)$	$-\frac{\sqrt{3}}{2}xy - \frac{1}{4}(x^2 - y^2)$
$C_3(\frac{-4\pi}{3})$	$-\frac{1}{2}x - \frac{\sqrt{3}}{2}y$	$\frac{\sqrt{3}}{2}x + \frac{1}{2}y$	z	z^2	$-\frac{1}{2}xy - \frac{\sqrt{3}}{4}(x^2 + y^2)$	$\frac{\sqrt{3}}{2}xy - \frac{1}{4}(x^2 - y^2)$
σ_ν	$-x$	y	z	z^2	$-xy$	$\frac{1}{2}(x^2 - y^2)$
σ_ν'	$\frac{1}{2}x - \frac{\sqrt{3}}{2}$	$-\frac{\sqrt{3}}{2}x - \frac{1}{2}y$	z	z^2	$\frac{1}{2}xy - \frac{\sqrt{3}}{4}(x^2 + y^2)$	$-\frac{\sqrt{3}}{2}xy - \frac{1}{4}(x^2 - y^2)$
σ_ν''	$\frac{1}{2}x + \frac{\sqrt{3}}{2}$	$\frac{\sqrt{3}}{2}x - \frac{1}{2}y$	z	z^2	$\frac{1}{2}xy + \frac{\sqrt{3}}{4}(x^2 + y^2)$	$\frac{\sqrt{3}}{2}xy - \frac{1}{4}(x^2 - y^2)$

Table 2.1: Some symmetry operators of the D_{3h} point group on basis functions taking (x, y, z) into (x', y', z'). $C_3(\frac{-2\pi}{3})$ and $C_3(\frac{-4\pi}{3})$ are the rotaions by $\frac{-2\pi}{3}$ and $\frac{-4\pi}{3}$ around the z axis, respectively. σ_ν is the reflection angular bisector of R_1 and R_6 in Fig. , and $\sigma_\nu', \sigma_\nu''$ are obtained through rotating σ_ν around the z axis by $2\pi/3$ and $4\pi/3$, respectively.

One parameterizes the matrices $\mathcal{E}(\mathbf{0})$ and $\mathcal{E}(\mathbf{R}_1)$ by

$$
\mathcal{E}(\mathbf{0}) = \begin{pmatrix} \epsilon_1 & 0 & 0 \\ 0 & \epsilon_1 & 0 \\ 0 & 0 & \epsilon_2 \end{pmatrix},
$$
$$
\mathcal{E}(\mathbf{R}_1) = \begin{pmatrix} t_0 & t_1 & t_2 \\ -t_1 & t_{11} & t_{12} \\ t_2 & -t_{12} & t_{22} \end{pmatrix}.
\tag{2.11}
$$

Given $\mathcal{E}(\mathbf{R}_1)$, the matrix $\mathcal{E}(\mathbf{R}_{2-6})$ corresponding to all neighbor sites $\mathbf{R}_{2-6}$ can be gen-

erated by

$$\mathcal{E}(g_n \mathbf{R}_1) = D(g_n)\mathcal{E}(\mathbf{R}_1)D^\dagger(g_n), \tag{2.12}$$

where $D(g_n)$ is the matrix of the irreducible representation, g_n are symmetry operators of D_{3h} point groups, $\{E, 2C_3, 3C_2, 2S_3, \sigma_h, 3\sigma_\nu\}$. Particularly, we have $\mathcal{E}(\mathbf{R}_2) = \mathcal{E}(\sigma'_\nu \mathbf{R}_1)$, $\mathcal{E}(\mathbf{R}_3) = \mathcal{E}(C_3(-\frac{2\pi}{3})\mathbf{R}_1)$, $\mathcal{E}(\mathbf{R}_4) = \mathcal{E}(\sigma_\nu \mathbf{R}_1)$, $\mathcal{E}(\mathbf{R}_5) = \mathcal{E}(C_3(-\frac{4\pi}{3}\mathbf{R}_1)$, $\mathcal{E}(\mathbf{R}_6) = \mathcal{E}(\sigma''_\nu \mathbf{R}_1)$. Table 2.1 depicts the transformation of the basis functions under the action of symmetry operators. Also, from Table 2.1, we obtain irreducible matrices as follows

$$D(C_3(-\tfrac{2\pi}{3})) = \begin{pmatrix} 1 & 0 & 0 \\ 0 & -1/2 & \sqrt{3}/2 \\ 0 & -\sqrt{3}/2 & -1/2 \end{pmatrix}, \quad D(C_3(-\tfrac{4\pi}{3})) = \begin{pmatrix} 1 & 0 & 0 \\ 0 & -1/2 & -\sqrt{3}/2 \\ 0 & \sqrt{3}/2 & -1/2 \end{pmatrix},$$

$$D(\sigma_\nu) = \begin{pmatrix} 1 & 0 & 0 \\ 0 & -1 & 0 \\ 0 & 0 & 0 \end{pmatrix}, \quad D(\sigma'_\nu) = \begin{pmatrix} 1 & 0 & 0 \\ 1 & 1/2 & -\sqrt{3}/2 \\ 0 & -\sqrt{3}/2 & -1/2 \end{pmatrix}, \tag{2.13}$$

$$D(\sigma''_\nu) = \begin{pmatrix} 1 & 0 & 0 \\ 0 & 1/2 & \sqrt{3}/2 \\ 0 & \sqrt{3}/2 & -1/2 \end{pmatrix}.$$

Therefore, we have

$$\begin{aligned}
\mathcal{E}(\mathbf{R}_2) &= D(\sigma'_\nu)\mathcal{E}(\mathbf{R}_1)D^\dagger(\sigma'_\nu) \\
&= \begin{pmatrix} t_0 & \frac{1}{2}t_1 - \frac{\sqrt{3}}{2}t_2 & -\frac{\sqrt{3}}{2}t_1 - \frac{1}{2}t_2 \\ -\frac{1}{2}t_1 - \frac{\sqrt{3}}{2}t_2 & \frac{1}{4}t_{11} + \frac{3}{4}t_{22} & -\frac{\sqrt{3}}{4}t_{11} - t_{12} + \frac{\sqrt{3}}{4}t_{22} \\ \frac{\sqrt{3}}{2}t_1 - \frac{1}{2}t_2 & -\frac{\sqrt{3}}{4}t_{11} + t_{12} + \frac{\sqrt{3}}{4}t_{22} & \frac{3}{4}t_{11} + \frac{1}{4}t_{22} \end{pmatrix},
\end{aligned} \tag{2.14}$$

$$\begin{aligned}
\mathcal{E}(\mathbf{R}_3) &= D(C(-\tfrac{2\pi}{3}))\mathcal{E}(\mathbf{R}_1)D^\dagger(C(-\tfrac{2\pi}{3})) \\
&= \begin{pmatrix} t_0 & -\frac{1}{2}t_1 + \frac{\sqrt{3}}{2}t_2 & -\frac{\sqrt{3}}{2}t_1 - \frac{1}{2}t_2 \\ \frac{1}{2}t_1 + \frac{\sqrt{3}}{2}t_2 & \frac{1}{4}t_{11} + \frac{3}{4}t_{22} & \frac{\sqrt{3}}{4}t_{11} + t_{12} - \frac{\sqrt{3}}{4}t_{22} \\ \frac{\sqrt{3}}{2}t_1 - \frac{1}{2}t_2 & \frac{\sqrt{3}}{4}t_{11} - t_{12} - \frac{\sqrt{3}}{4}t_{22} & \frac{3}{4}t_{11} + \frac{1}{4}t_{22} \end{pmatrix},
\end{aligned} \tag{2.15}$$

$$\mathcal{E}(\mathbf{R}_4) = D(\sigma_\nu)\mathcal{E}(\mathbf{R}_1)D^\dagger(\sigma_\nu) = \begin{pmatrix} t_0 & -t_1 & t_2 \\ t_1 & t_{11} & -t_{12} \\ t_2 & t_{12} & t_{22} \end{pmatrix}, \tag{2.16}$$

$$\mathcal{E}(\mathbf{R}_5) = D(C(-\tfrac{4\pi}{3}))\mathcal{E}(\mathbf{R}_1)D^\dagger(C(-\tfrac{4\pi}{3}))$$

$$= \begin{pmatrix} t_0 & -\tfrac{1}{2}t_1 - \tfrac{\sqrt{3}}{2}t_2 & \tfrac{\sqrt{3}}{2}t_1 - \tfrac{1}{2}t_2 \\ \tfrac{1}{2}t_1 - \tfrac{\sqrt{3}}{2}t_2 & \tfrac{1}{4}t_{11} + \tfrac{3}{4}t_{22} & -\tfrac{\sqrt{3}}{4}t_{11} + t_{12} + \tfrac{\sqrt{3}}{4}t_{22} \\ -\tfrac{\sqrt{3}}{2}t_1 - \tfrac{1}{2}t_2 & -\tfrac{\sqrt{3}}{4}t_{11} - t_{12} + \tfrac{\sqrt{3}}{4}t_{22} & \tfrac{3}{4}t_{11} + \tfrac{1}{4}t_{22} \end{pmatrix}, \tag{2.17}$$

$$\mathcal{E}(\mathbf{R}_6) = D(\sigma_\nu'')\mathcal{E}(\mathbf{R}_1)D^\dagger(\sigma_\nu'')$$

$$= \begin{pmatrix} t_0 & \tfrac{1}{2}t_1 + \tfrac{\sqrt{3}}{2}t_2 & \tfrac{\sqrt{3}}{2}t_1 - \tfrac{1}{2}t_2 \\ -\tfrac{1}{2}t_1 + \tfrac{\sqrt{3}}{2}t_2 & \tfrac{1}{4}t_{11} + \tfrac{3}{4}t_{22} & \tfrac{\sqrt{3}}{4}t_{11} - t_{12} - \tfrac{\sqrt{3}}{4}t_{22} \\ -\tfrac{\sqrt{3}}{2}t_1 - \tfrac{1}{2}t_2 & \tfrac{\sqrt{3}}{4}t_{11} - t_{12} - \tfrac{\sqrt{3}}{4}t_{22} & \tfrac{3}{4}t_{11} + \tfrac{1}{4}t_{22} \end{pmatrix}, \tag{2.18}$$

The nearest-neighbor tight-binding Hamiltonian now can be written as

$$H^{\mathrm{NN}}(\mathbf{k}) = \begin{pmatrix} h_0 & h_1 & h_2 \\ h_1^* & h_{11} & h_{12} \\ h_2^* & h_{12}^* & h_{22} \end{pmatrix} \tag{2.19}$$

where

$$\begin{aligned}
h_0 &= 2t_0\left(\cos 2\alpha + 2\cos\alpha\cos\beta\right) + \epsilon_1, \\
h_1 &= 2it_1(\sin 2\alpha + \sin\alpha\cos\beta) - 2\sqrt{3}t_2\sin\alpha\sin\beta, \\
h_2 &= 2t_2(\cos 2\alpha - \cos\alpha\cos\beta) + 2i\sqrt{3}t_1\cos\alpha\sin\beta, \\
h_{11} &= (t_{11} + 3t_{22})\cos\alpha\cos\beta + 2t_{11}\cos 2\alpha + \epsilon_2, \\
h_{22} &= (3t_{11} + t_{22})\cos\alpha\cos\beta + 2t_{22}\cos 2\alpha + \epsilon_2, \\
h_{12} &= \sqrt{3}(t_{22} - t_{11})\sin\alpha\sin\beta + 4it_{12}\sin\alpha(\cos\alpha - \cos\beta),
\end{aligned} \tag{2.20}$$

$$(\alpha, \beta) = \left(\tfrac{1}{2}k_x a, \tfrac{\sqrt{3}}{2}k_y a\right). \tag{2.21}$$

Eight additional parameters depicted in Table 2.2 are obtained by fitting the band with *ab initio* calculation results.

	$a(\text{Å})$	ϵ_1	ϵ_2	t_0	t_1	t_2	t_{11}	t_{12}	t_{22}
MoS_2	3.190	1.046	2.104	-0.184	0.401	0.507	0.218	0.338	0.057
WS_2	3.191	1.130	2.275	-0.206	0.567	0.536	0.286	0.384	-0.061
$MoSe_2$	3.326	0.919	2.065	-0.188	0.317	0.456	0.211	0.290	0.130
WSe_2	3.325	0.943	2.179	-0.207	0.457	0.486	0.263	0.329	0.034
$MoTe_2$	3.557	0.605	1.972	-0.169	0.228	0.390	0.207	0.239	0.252
WTe_2	3.560	0.606	2.102	-0.175	0.342	0.410	0.233	0.270	0.190

Table 2.2: Fitted parameters in three-band NN TBM for generalized-gradient approximation (GGA) cases for MX_2 [1].
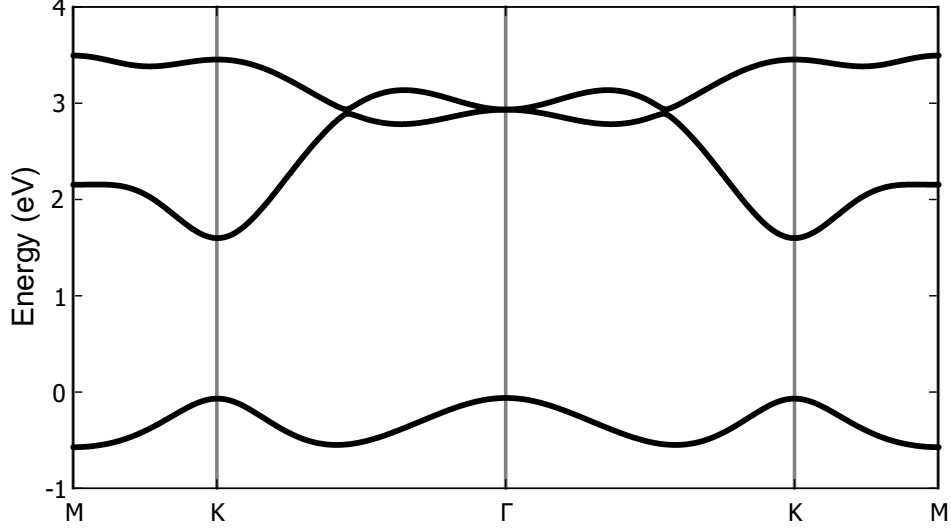
Figure 2.2: To obtain the band structure of monolayer MoS_2, the eigenvalue of the Hamiltonian needs to be found at each k point across the entire the Brillouin zone (BZ). This figure illustrates the band structure along Γ-K direction using (GGA) fitting parameters.

2.2 Three-band tight binding method under a magnetic field

Under a uniform magnetic field given by a vector potential $\mathbf{A}(\mathbf{r})$ the single electron Hamiltonian changes into

$$H = \frac{\left(-i\hbar\boldsymbol{\nabla} + e\mathbf{A}(\mathbf{r})\right)^2}{2m} + U_0(\mathbf{r}) + g^*\mu_B\mathbf{B}\cdot\mathbf{L}, \tag{2.22}$$

where $\mu_B = \dfrac{e\hbar}{2m}$ is Bohr magneton, g^* is an effective Landé g-factor, $\mathbf{B} = \boldsymbol{\nabla}\times\mathbf{A}$ is the uniform magnetic field, and $\mathbf{L}$ is the angular momentum. It is possible to add a phase factor to the tight binding wavefunction

$$\psi_{\lambda,\mathbf{k}}(\mathbf{r}) = \sum_{j=1}^{3} C_j'^{\lambda}(\mathbf{k}) \sum_{\mathbf{R}} e^{i\mathbf{k}\cdot\mathbf{R}}e^{\theta_{\mathbf{R}}(\mathbf{r})}\phi_j(\mathbf{r} - \mathbf{R}). \tag{2.23}$$

We now have

$$H_{jj'}(\mathbf{k}) = H_{jj'}^{\mathrm{NN}}(\mathbf{k}) + H_{jj'}^{Z}(\mathbf{k}), \tag{2.24}$$

where

$$H_{jj'}^{\mathrm{NN}}(\mathbf{k}) = \sum_{\mathbf{R}} \langle \phi_j(\mathbf{r})| \, e^{-i\theta_{\mathbf{0}}(\mathbf{r})} \left[\frac{(-i\hbar\boldsymbol{\nabla} + e\mathbf{A}(\mathbf{r}))^2}{2m} + U_0(\mathbf{r}) \right] e^{i\mathbf{k}\cdot\mathbf{R}} e^{\theta_{\mathbf{R}}(\mathbf{r})} \, |\phi_{j'}(\mathbf{r}-\mathbf{R})\rangle$$

$$= \sum_{\mathbf{R}} \langle \phi_j(\mathbf{r})| \, e^{i(\mathbf{k}\cdot\mathbf{R} + \theta_{\mathbf{R}} - \theta_{\mathbf{0}})} \left[\frac{(-i\hbar\boldsymbol{\nabla} + e\mathbf{A} + \hbar\boldsymbol{\nabla}\theta_{\mathbf{R}})^2}{2m} + U_0(\mathbf{r}) \right] |\phi_{j'}(\mathbf{r}-\mathbf{R})\rangle,$$

$$(2.25)$$

and

$$H_{jj'}^{Z}(\mathbf{k}) = g^*\mu_B \mathbf{B} \cdot \sum_{\mathbf{R}} \langle \phi_j(\mathbf{r})| \, e^{i(\mathbf{k}\cdot\mathbf{R} + \theta_{\mathbf{R}} - \theta_{\mathbf{0}})} \mathbf{L} \, |\phi_{j'}(\mathbf{r}-\mathbf{R})\rangle. \qquad (2.26)$$

By choosing $\theta_{\mathbf{R}} = -\frac{e}{\hbar}\int_{\mathbf{R}}^{\mathbf{r}} \mathbf{A}(\mathbf{r}')\cdot d\mathbf{r}'$ as Peierls substitution, the Hamiltonian in Eq. (2.25) now reads

$$H_{jj'}^{\mathrm{NN}}(\mathbf{k}) = \sum_{\mathbf{R}} \langle \phi_j(\mathbf{r})| \, e^{i\mathbf{k}\cdot\mathbf{R} - \frac{ie}{\hbar}\int_{\mathbf{R}}^{\mathbf{r}} \mathbf{A}(\mathbf{r}')\cdot d\mathbf{r}' + \frac{ie}{\hbar}\int_{\mathbf{0}}^{\mathbf{r}} \mathbf{A}(\mathbf{r}')\cdot d\mathbf{r}'} \left[-\frac{\hbar^2\boldsymbol{\nabla}^2}{2m} + U_0(\mathbf{r}) \right] |\phi_{j'}(\mathbf{r}-\mathbf{R})\rangle$$

$$= \sum_{\mathbf{R}} e^{i\mathbf{k}\cdot\mathbf{R}} e^{\frac{ie}{\hbar}\int_{\mathbf{0}}^{\mathbf{R}} \mathbf{A}(\mathbf{r}')\cdot d\mathbf{r}'} \langle \phi_j(\mathbf{r})| \, e^{-\frac{ie}{\hbar}\Phi_{\mathbf{R},\mathbf{r},\mathbf{0}}} \left[-\frac{\hbar^2\boldsymbol{\nabla}^2}{2m} + U_0(\mathbf{r}) \right] |\phi_{j'}(\mathbf{r}-\mathbf{R})\rangle,$$

where $\Phi_{\mathbf{R},\mathbf{r},\mathbf{0}} = \oint_{\mathbf{R},\mathbf{r},\mathbf{0}} \mathbf{A}(\mathbf{r}')\cdot d\mathbf{r}'$ is the closed loop line integral of $\mathbf{A}$ along the triangle points $\mathbf{R}, \mathbf{r}, \mathbf{0}$, and $\int_{\mathbf{0}}^{\mathbf{R}} \mathbf{A}(\mathbf{r}')\cdot d\mathbf{r}'$ is the path integral along the two points $\mathbf{R}, \mathbf{0}$. Besides that, we have used the fact that

$$\int_{\mathbf{R}}^{\mathbf{r}} \mathbf{A}(\mathbf{r}')\cdot d\mathbf{r}' + \int_{\mathbf{r}}^{\mathbf{0}} \mathbf{A}(\mathbf{r}')\cdot \mathbf{r}' = \Phi_{\mathbf{R},\mathbf{r},\mathbf{0}} - \int_{\mathbf{0}}^{\mathbf{R}} \mathbf{A}(\mathbf{r}')\cdot d\mathbf{r}'. \qquad (2.27)$$

We can show that the flux term $\Phi_{\mathbf{R},\mathbf{r},\mathbf{0}}$ is negligibly small [2] by two observations. When $\mathbf{r}$ is far away from the lattice points $\mathbf{R}$ and $\mathbf{0}$, the flux is large but since the atomic orbitals are highly localized at these two lattice points, the value of the hopping term is very small and the whole hopping term goes to zero. While $\mathbf{r}$ is at or near any of these lattice points, the triangle formed is small, and assuming small magnetic field, the flux term $\Phi_{\mathbf{R},\mathbf{r},\mathbf{0}}$ goes to zero, which giving us the Hamiltonian as

$$H_{jj'}^{\mathrm{NN}}(\mathbf{k}) = \sum_{\mathbf{R}} e^{i\mathbf{k}\cdot\mathbf{R}} e^{\frac{ie}{\hbar}\int_{\mathbf{0}}^{\mathbf{R}} \mathbf{A}(\mathbf{r}')\cdot d\mathbf{r}'} \langle \phi_j(\mathbf{r})| \left[-\frac{\hbar^2\boldsymbol{\nabla}^2}{2m} + U_0(\mathbf{r}) \right] |\phi_{j'}(\mathbf{r}-\mathbf{R})\rangle, \qquad (2.28)$$

$$H_{jj'}^{Z}(\mathbf{k}) = g^*\mu_B \mathbf{B} \cdot \sum_{\mathbf{R}} e^{i\mathbf{k}\cdot\mathbf{R}} e^{\frac{ie}{\hbar}\int_{\mathbf{0}}^{\mathbf{R}} \mathbf{A}(\mathbf{r}')\cdot d\mathbf{r}'} \langle \phi_j(\mathbf{r})| \, \mathbf{L} \, |\phi_{j'}(\mathbf{r}-\mathbf{R})\rangle. \qquad (2.29)$$

Considering only NN hopping, Eq (2.29) becomes

$$
\begin{aligned}
H_{jj'}^{\text{NN}}(\mathbf{k}) &= \sum_{\mathbf{R}} e^{i\mathbf{k}\cdot\mathbf{R}} e^{\frac{e}{\hbar}\int_0^{\mathbf{R}} A(\mathbf{r}')d\mathbf{r}'} \mathcal{E}_{jj'}(\mathbf{R}) \\
&= \mathcal{E}_{jj'}(\mathbf{0}) + e^{i\mathbf{k}\cdot\mathbf{R_1}} e^{\frac{e}{\hbar}\int_0^{\mathbf{R_1}} A(\mathbf{r}')d\mathbf{r}'} \mathcal{E}_{jj'}(\mathbf{R_1}) \\
&\quad + e^{i\mathbf{k}\cdot\mathbf{R_2}} e^{\frac{e}{\hbar}\int_0^{\mathbf{R_2}} A(\mathbf{r}')d\mathbf{r}'} \mathcal{E}_{jj'}(\mathbf{R_2}) + e^{i\mathbf{k}\cdot\mathbf{R_3}} e^{\frac{e}{\hbar}\int_0^{\mathbf{R_3}} A(\mathbf{r}')d\mathbf{r}'} \mathcal{E}_{jj'}(\mathbf{R_3}) \\
&\quad + e^{i\mathbf{k}\cdot\mathbf{R_3}} e^{\frac{e}{\hbar}\int_0^{\mathbf{R_3}} A(\mathbf{r}')d\mathbf{r}'} \mathcal{E}_{jj'}(\mathbf{R_4}) + e^{i\mathbf{k}\cdot\mathbf{R_5}} e^{\frac{e}{\hbar}\int_0^{\mathbf{R_5}} A(\mathbf{r}')d\mathbf{r}'} \mathcal{E}_{jj'}(\mathbf{R_5}) \\
&\quad + e^{i\mathbf{k}\cdot\mathbf{R_6}} e^{\frac{e}{\hbar}\int_0^{\mathbf{R_6}} A(\mathbf{r}')d\mathbf{r}'} \mathcal{E}_{jj'}(\mathbf{R_6}).
\end{aligned}
\tag{2.30}
$$

In the presence of a perpendicular magnetic field $\mathbf{B}\hat{z}$ applied to the plane of TMD, we choose the vector potential in the Landau gauge as $\mathbf{A} = (0, Bx, 0)$. For convenience, let us define a shorthand notation for these extra terms

$$
\begin{aligned}
\theta_{m,n}^{m',n'} &= \frac{e}{\hbar}\int_{m,n}^{m',n'} \mathbf{A}(\mathbf{r}) \cdot d\mathbf{r} \\
&= \frac{eB}{2\hbar}(x_m + x_{m'})(y_{n'} - y_n),
\end{aligned}
\tag{2.31}
$$

in which $x_m = \frac{ma}{2}(m = \pm 1, \pm 2)$ and $y_n = \frac{na\sqrt{3}}{2}(n = 0, \pm 1)$ are the NN coordinates and a being the lattice constant, are shown in Fig.(2.3). Details of this calculation is given in Appendix A.
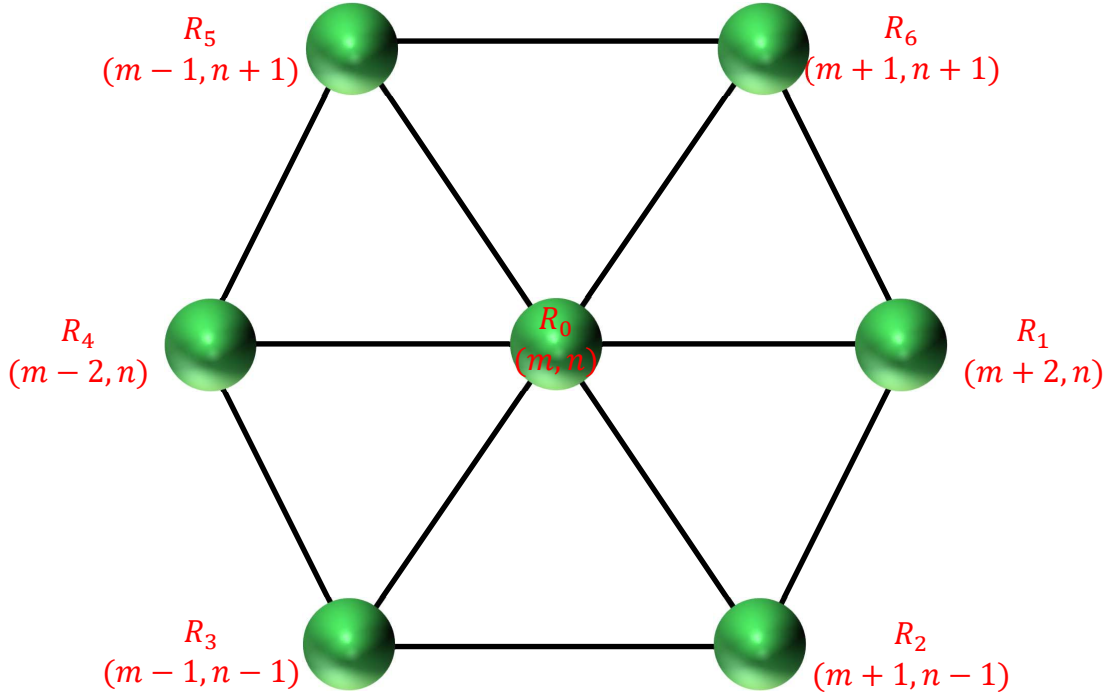

Figure 2.3: The TBM of TMD with six neighbors atom M rewrite with the site index.

Since $dy = 0$ along the x direction, $\theta_{m,n}^{m\pm 2,n} = 0$, and using NN coordinates given for

lattice site, the $\theta_{m,n}^{m',n'}$ can be written as

$$\theta_{m,n}^{m',n'} = \begin{cases} 0 & m' = m \pm 2, n' = n, \\ \pm\frac{e}{\hbar}\frac{Ba^2\sqrt{3}}{4}(m+1/2) & m' = m+1, n' = n \pm 1, \\ \pm\frac{e}{\hbar}\frac{Ba^2\sqrt{3}}{4}(m-1/2) & m' = m-1, n' = n \pm 1. \end{cases} \quad (2.32)$$

Identifying $\frac{Ba^2\sqrt{3}}{4}$ as the magnetic flux Φ passing through per unit cell and $\frac{h}{e}$ corresponds to the magnetic flux quantum Φ_0, we obtain the following relation:

$$\begin{aligned} H_{jj'}(\mathbf{k}) &= E_{jj'}(\mathbf{0}) + e^{i\mathbf{k}\cdot\mathbf{R}_1}E_{jj'}(\mathbf{R}_1) + e^{-2i\pi(m+1/2)\Phi/\Phi_0}e^{i\mathbf{k}\cdot\mathbf{R}_2}E_{jj'}(\mathbf{R}_2) \\ &+ e^{-2i\pi(m-1/2)\Phi/\Phi_0}e^{i\mathbf{k}\cdot\mathbf{R}_3}E_{jj'}(\mathbf{R}_3) + e^{i\mathbf{k}\cdot\mathbf{R}_4}E_{jj'}(\mathbf{R}_4) \\ &+ e^{2i\pi(m-1/2)\Phi/\Phi_0}e^{i\mathbf{k}\cdot\mathbf{R}_5}E_{jj'}(\mathbf{R}_5) + e^{2i\pi(m+1/2)\Phi/\Phi_0}e^{i\mathbf{k}\cdot\mathbf{R}_6}E_{jj'}(\mathbf{R}_6). \end{aligned} \quad (2.33)$$

The Hamiltonian depends only on the site index m and does not invariant under the expansion of a lattice vector along the x axis. In order to restore this invariance, we can look at the case where the ratio of magnetic flux and flux quanta is a rational number $\Phi/\Phi_0 = p/q$. The crucial advantage of the Peierls phase approach is alowed the lattice periodicity can be restored provided a suitable "magnetic supercell" containing several original unit cells is constructed. One might ask what actually happens inside the magnetic unit cells? Do the NN still interact in the same way as they did in the tight-binding model? We will focus in this after we get the Hamiltonian for the magnetic unit cell.

The magnetic unit cell has lattice vectors $q\mathbf{a}_1$ and $\mathbf{a}_2$ is illustrated in Fig.
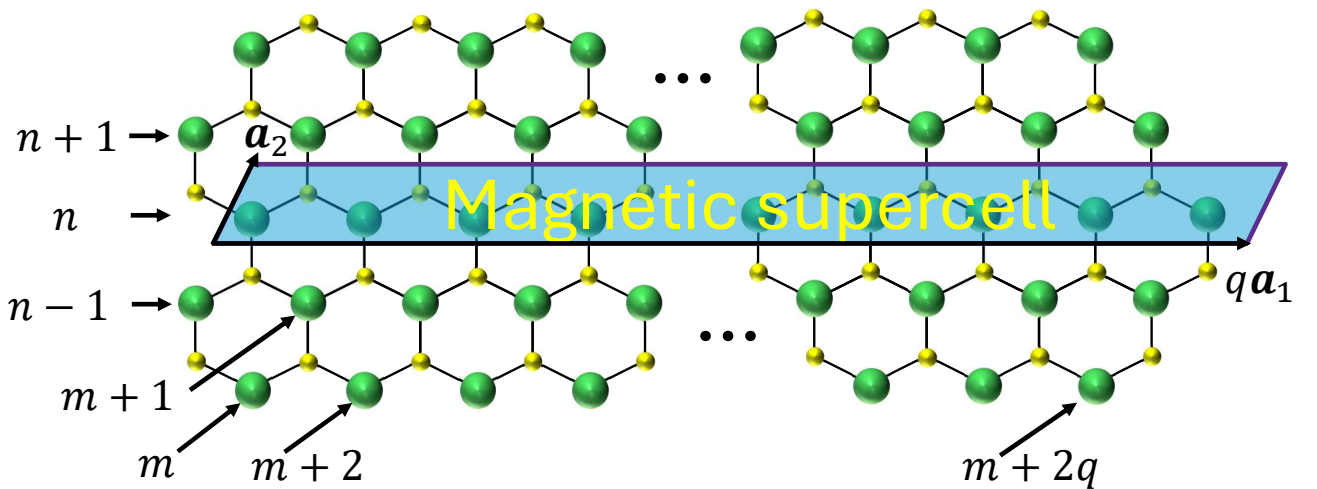

Figure 2.4: Magnetic unit cell for TMD monolayers.

In Section 2.1, we have ignore the sum over of relative positions $\mathbf{r}_c$ in Eq (2.2) due to ignore the orbitals of X atoms. While, the magnetic unit cell consits $2q$ atom M.

We, now, define a new basis set of $6q$ atomic orbitals $\{\phi_j(\mathbf{r} - \mathbf{r}_i)\}$ where $j = 1, 2, 3$ and $i = 1, 2, ..., 2q$. The new basis function now is

$$\psi_{\lambda,\mathbf{k}}(\mathbf{r}) = \sum_{j,i} C_{ji}^{\lambda}(\mathbf{k}) \sum_{\alpha}^{N_{\text{UC}}} e^{i\mathbf{k}\cdot(\mathbf{R}_{\alpha}+\mathbf{r}_i)} \phi_j(\mathbf{r} - \mathbf{R}_{\alpha} - \mathbf{r}_i). \tag{2.34}$$

Here, we set $\mathbf{r}_i$ refers to the position of an atom in a unit cell, while $\mathbf{R}_{\alpha}$ denotes the position of different unit cells. The Hamiltonian matrix elements in the new basis is written as

$$H_{jj'}^{ii'}(\mathbf{k}) = \sum_{\alpha}^{N_{\text{UC}}} \sum_{\beta}^{N_{\text{UC}}} e^{i\mathbf{k}\cdot(\mathbf{R}_{\beta}-\mathbf{R}_{\alpha}+\mathbf{r}_{i'}-\mathbf{r}_i)} \left\langle \phi_j(\mathbf{r} - \mathbf{R}_{\alpha} - \mathbf{r}_i) \right| \left[-\frac{\hbar^2 \boldsymbol{\nabla}^2}{2m} + U_0 \right] \left| \phi_j(\mathbf{r} - \mathbf{R}_{\beta} - \mathbf{r}_{i'}) \right\rangle. \tag{2.35}$$

Now we center our system at $\mathbf{r}' = \mathbf{r} - \mathbf{R}_{\alpha} - \mathbf{r}_i$ and define $\mathbf{R}_{\gamma} = \mathbf{R}_{\alpha} - \mathbf{R}_{\beta}$. This leads to

$$H_{jj'}^{ii'}(\mathbf{k}) = \sum_{\alpha}^{N_{\text{UC}}} \sum_{\gamma}^{N_{\text{UC}}} e^{-i\mathbf{k}\cdot(\mathbf{R}_{\gamma}+\mathbf{r}_i-\mathbf{r}_{i'})} \left\langle \phi_j(\mathbf{r}) \right| \left[-\frac{\hbar^2 \boldsymbol{\nabla}^2}{2m} + U_0 \right] \left| \phi_j(\mathbf{r} + \mathbf{R}_{\gamma} + \mathbf{r}_i - \mathbf{r}_{i'}) \right\rangle. \tag{2.36}$$

Taking the sum over $\mathbf{R}$ and replacing $\mathbf{r}_i = m\mathbf{a}_1 + n\mathbf{a}_2$, $\mathbf{r}_{i'} = m'\mathbf{a}_1 + n'\mathbf{a}_2$, notice that $i = (m, n)$ with only considering the nearest-neighbors, we define our hopping terms in the new basis is given by

$$H_{ii'}^{jj'}(\mathbf{k}) = \sum_{\alpha}^{N_{\text{UC}}} \sum_{\gamma}^{N_{\text{UC}}} e^{-i\mathbf{k}\cdot\mathbf{R}_{\gamma}} \left\langle \phi_j(\mathbf{r}) \right| \left[-\frac{\hbar^2 \boldsymbol{\nabla}^2}{2m} + U_0(\mathbf{r}) \right] \left| \phi_{j'}(\mathbf{r} + \mathbf{R}_{\gamma}) \right\rangle \delta_{i,i'}. \tag{2.37}$$

One can regconize that Eq. (2.37) resembles Eq. (2.6). Additionally, the equation not only describes the hopping between magnetic unit cells but also accounts for hopping between sites within magnetic unit cells. To address the previous question, it is important to note that we have enlarged the original unit cell into a magnetic unit cell, which now contains $2q$ atoms M. The NN interactions are preserved inside the "supercell", but they now involve neighboring magnetic unit cells due to the enlarged cell structure. The Hamiltonian has a discrete tranlastional invariance with a unit cell carrying $2q$ unit cells along the x axis.

We can choose $\mathbf{R}_{\beta} = \mathbf{0}$, this will not affect the Hamiltonian because the sum over $\mathbf{R}$ is

only considering the NN atoms, Hamiltonian with the Peierls phase now is

$$
\begin{aligned}
H_{jj'}^{ii'}(\mathbf{k}) &= e^{i\theta_{m,n}^{m,n}} e^{i\mathbf{k}\cdot(\mathbf{0}-\mathbf{0})} \left\langle \phi_j(\mathbf{r}) \right| \left[-\frac{\hbar^2\boldsymbol{\nabla}^2}{2m} + U_0(\mathbf{r}) \right] \left| \phi_{j'}(\mathbf{r}) \right\rangle \delta_{m',m}^{n',n} \\
&+ e^{i\theta_{m,n}^{m+2,n}} e^{i\mathbf{k}\cdot(\mathbf{0}-\mathbf{R}_1)} \left\langle \phi_j(\mathbf{r}) \right| \left[-\frac{\hbar^2\boldsymbol{\nabla}^2}{2m} + U_0(\mathbf{r}) \right] \left| \phi_{j'}(\mathbf{r}-\mathbf{R}_1) \right\rangle \delta_{m,m+2}^{n',n} \\
&+ e^{i\theta_{m,n}^{m-2,n}} e^{i\mathbf{k}\cdot(\mathbf{0}-\mathbf{R}_4)} \left\langle \phi_j(\mathbf{r}) \right| \left[-\frac{\hbar^2\boldsymbol{\nabla}^2}{2m} + U_0(\mathbf{r}) \right] \left| \phi_{j'}(\mathbf{r}-\mathbf{R}_4) \right\rangle \delta_{m',m-2}^{n',n} \\
&+ e^{i\theta_{m,n}^{m+1,n-1}} e^{i\mathbf{k}\cdot(\mathbf{0}-\mathbf{R}_2)} \left\langle \phi_j(\mathbf{r}) \right| \left[-\frac{\hbar^2\boldsymbol{\nabla}^2}{2m} + U_0(\mathbf{r}) \right] \left| \phi_{j'}(\mathbf{r}-\mathbf{R}_2) \right\rangle \delta_{m',m+1}^{n',n-1} \quad (2.38) \\
&+ e^{i\theta_{m,n}^{m-1,n-1}} e^{i\mathbf{k}\cdot(\mathbf{0}-\mathbf{R}_3)} \left\langle \phi_j(\mathbf{r}) \right| \left[-\frac{\hbar^2\boldsymbol{\nabla}^2}{2m} + U_0(\mathbf{r}) \right] \left| \phi_{j'}(\mathbf{r}-\mathbf{R}_3) \right\rangle \delta_{m',m-1}^{n',n-1} \\
&+ e^{i\theta_{m,n}^{m-1,n+1}} e^{i\mathbf{k}\cdot(\mathbf{0}-\mathbf{R}_5)} \left\langle \phi_j(\mathbf{r}) \right| \left[-\frac{\hbar^2\boldsymbol{\nabla}^2}{2m} + U_0(\mathbf{r}) \right] \left| \phi_{j'}(\mathbf{r}-\mathbf{R}_5) \right\rangle \delta_{m',m-1}^{n',n+1} \\
&+ e^{i\theta_{m,n}^{m+1,n+1}} e^{i\mathbf{k}\cdot(\mathbf{0}-\mathbf{R}_6)} \left\langle \phi_j(\mathbf{r}) \right| \left[-\frac{\hbar^2\boldsymbol{\nabla}^2}{2m} + U_0(\mathbf{r}) \right] \left| \phi_{j'}(\mathbf{r}-\mathbf{R}_6) \right\rangle \delta_{m',m+1}^{n',n+1}.
\end{aligned}
$$

Simplizing Eq. (2.38), we get the Hamiltonian for the magnetic unit cell

$$
\begin{aligned}
H_{ii'}^{jj'}(\mathbf{k}) &= \mathcal{E}_{jj'}(\mathbf{0})\delta_{m',m}^{n',n} + e^{-i\mathbf{k}\cdot\mathbf{R}_1}\mathcal{E}_{jj'}(\mathbf{R}_1)\delta_{m',m+2}^{n',n} + e^{-i\mathbf{k}\cdot\mathbf{R}_4}\mathcal{E}_{jj'}(\mathbf{R}_4)\delta_{m',m-2}^{n',n} \\
&+ e^{-2i\pi(m+1/2)p/q}e^{-i\mathbf{k}\cdot\mathbf{R}_2}\mathcal{E}_{jj'}(\mathbf{R}_2)\delta_{m',m+1}^{n',n-1} + e^{-2i\pi(m-1/2)p/q}e^{-i\mathbf{k}\cdot\mathbf{R}_3}\mathcal{E}_{jj'}(\mathbf{R}_3)\delta_{m',m-1}^{n',n-1} \\
&+ e^{2i\pi(m-1/2)p/q}e^{-i\mathbf{k}\cdot\mathbf{R}_5}\mathcal{E}_{jj'}(\mathbf{R}_5)\delta_{m',m-1}^{n',n+1} + e^{2i\pi(m+1/2)p/q}e^{-i\mathbf{k}\cdot\mathbf{R}_6}\mathcal{E}_{jj'}(\mathbf{R}_6)\delta_{m',m+1}^{n',n+1}.
\end{aligned}
$$
(2.39)

Now, for given flux ratio p/q, only the q determines the periodicity of the magnetic cell assuming p and q are mutually prime numbers. When we plot the band energies while varying the p, we obtain the famous Hofstadter butterfly [3], a complex fractal structure as seen in Fig.(2.6). This structure is generated at the $K-$point. This fractal spectrum is a result of two competing effects, lattice periodicity and magnectic unit cell periodicity enforced by the presence of the magnetic field. Eq. (2.39) give the following matrix which must be diagonalized to obtain the energy eigenvalues

$$
H = \begin{pmatrix} h_0 & h_1 & h_2 \\ h_1^* & h_{11} & h_{12} \\ h_2^* & h_{12}^* & h_{22} \end{pmatrix}, \tag{2.40}
$$

with

$$
H_{jj'} = \begin{pmatrix}
\mathcal{E}_{jj'}(\mathbf{0}) & A_{jj'}^{(1)} & \mathcal{E}_{jj'}(\mathbf{R}_1) & 0 & \cdots & 0 & \mathcal{E}_{jj'}(\mathbf{R}_4) & B_{jj'}^{(1)} \\
B_{jj'}^{(2)} & \mathcal{E}_{jj'}(\mathbf{0}) & A_{jj'}^{(2)} & \mathcal{E}_{jj'}(\mathbf{R}_1) & 0 & \cdots & 0 & \mathcal{E}_{jj'}(\mathbf{R}_4) \\
\mathcal{E}_{jj'}(\mathbf{R}_4) & B_{jj'}^{(3)} & \mathcal{E}_{jj'}(\mathbf{0}) & A_{jj'}^{(3)} & \mathcal{E}_{jj'}(\mathbf{R}_1) & 0 & \cdots & 0 \\
\vdots & \vdots & \vdots & \ddots & \vdots & \vdots & \vdots & \vdots \\
\mathcal{E}_{jj'}(\mathbf{R}_1) & 0 & \cdots & 0 & \mathcal{E}_{jj'}(\mathbf{R}_4) & B_{jj'}^{(q-2)} & \mathcal{E}_{jj'}(\mathbf{0}) & A_{jj'}^{(q-2)} \\
A_{jj'}^{(q-1)} & \mathcal{E}_{jj'}(\mathbf{R}_1) & \cdots & 0 & 0 & \mathcal{E}_{jj'}(\mathbf{R}_4) & B_{jj'}^{(q-1)} & \mathcal{E}_{jj'}(\mathbf{0})
\end{pmatrix},
$$

(2.41)

where $A_{jj'}^{(m)} = \mathcal{E}_{jj'}(\mathbf{R}_2)e^{-2i\pi(m+1/2)p/q}e^{-i\mathbf{k}\cdot\mathbf{R}_2} + \mathcal{E}_{jj'}(\mathbf{R}_6)e^{2i\pi(m+1/2)p/q}e^{-i\mathbf{k}\cdot\mathbf{R}_6}$, and $B_{jj'}^{(m)} = \mathcal{E}_{jj'}(\mathbf{R}_3)e^{-2i\pi(m-1/2)p/q}e^{-i\mathbf{k}\cdot\mathbf{R}_3} + \mathcal{E}_{jj'}(\mathbf{R}_5)e^{2i\pi(m-1/2)p/q}e^{-i\mathbf{k}\cdot\mathbf{R}_5}$ and $h_0, h_1, h_2, h_{11}, h_{12}, h_{22}$ are submatrices of size $3q \times 3q$. (A visualization is shown in Fig. (2.5))
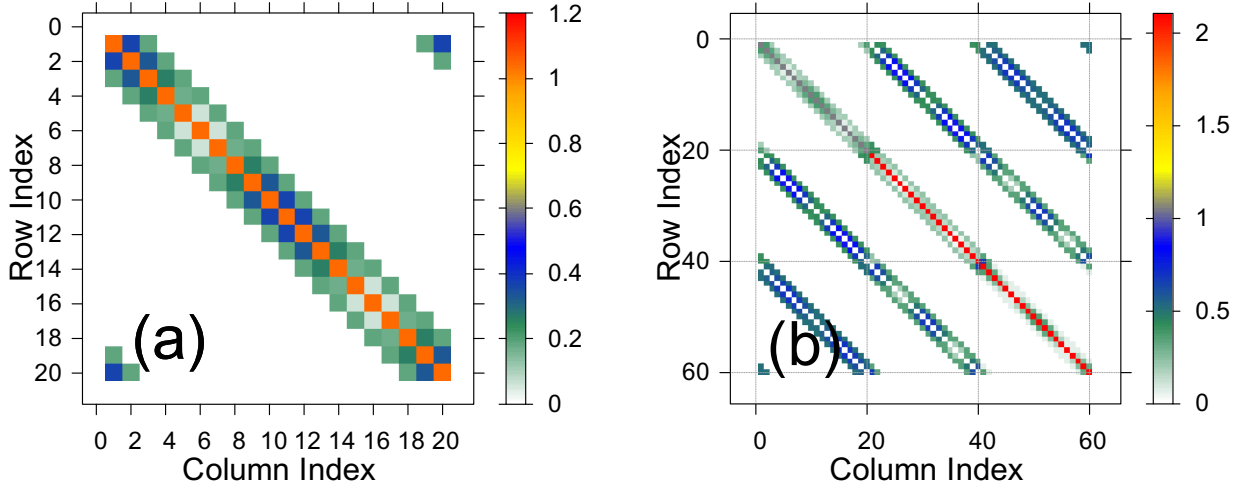

Figure 2.5: An simple and intuitive visualization of sub-matrix h_0 for single-band(a) and matrix H for three band(b) using standard plotter with $q = 20$. (a): orange squares, blue squares and green squares correspond to $\epsilon_1, 2t_0\cos\zeta_1, t_0$, respectively.

The magnetic field enters the TB Hamiltonian only through the fraction p/q, which is the magnetic flux through the primitive unit cell of the lattice. In general, as the lattice geometry evolves, the area of the primitive unit cell changes m times.

Another observation is that the lattice constant a and the magnetic field B always appears together in an expression with the magnetic field $(\frac{Ba^2\sqrt{3}}{4})$. This quantity reflects the flux per plaquette in the super magnetic unit cell, which is relevant is the context of Aharonov-Bohm effect [4]. Since the expression involves the product Ba^2, this implies that increasing B by a certain amount is mathematically equivalent to increasing a. In other words, for energy calculations, increasing the strength of the magnetic field is physically equivalent to increasing the lattice constant, as both affect the system in the same way through the flux per unit cell.

The spectrum exhibits several notable symmetries. First, it depends only on the
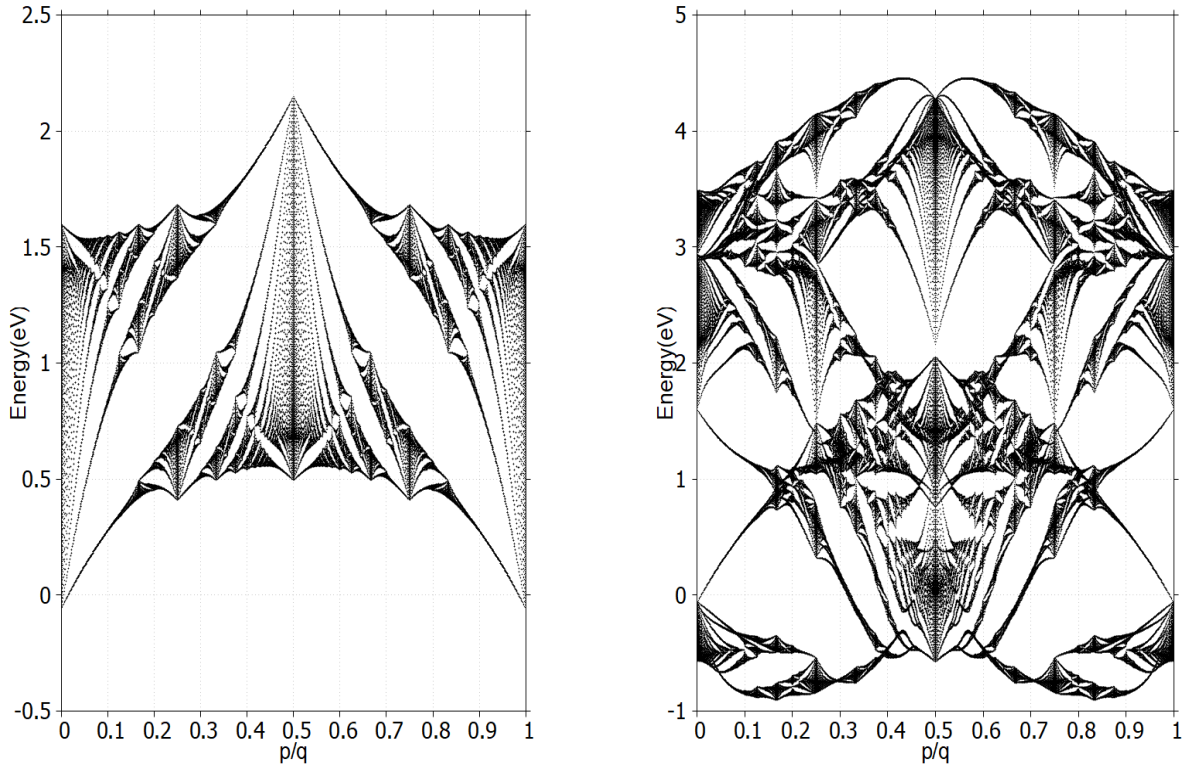
Figure 2.6: Hofstadter butterfly for single-band $|dz\rangle \equiv \left|\phi_1^1(x,y)\right\rangle$(left) and all band(right) with $q = 797$ and vary p from 1 to q with field strength $B_0 = 4.6928 \times 10^4$ T. Here on x−axis represents the flux in units of quantum flux enclosed by the unit cell and y−axis represents the Energy.

flux ratio p/q, meaning that shifting p/q by an integer c (i.e., $p/q \rightarrow p/q + c$) leaves the spectrum unchanged. Additionally, the spectrum remains invariant under the transformation $p/q \rightarrow -p/q$, since if ψ is an eigenstate with energy E for flux p/q, its complex conjugate ψ^* is an eigenstate with the same energy for flux $-p/q$. These two symmetries are general and not specific to the MX_2 case. The third symmetry involves changing p/q to $p/q + 1/2$, which is equivalent to flipping the sign of the hopping energies t_i (i.e., $t_i \rightarrow -t_i$), resulting in an inversion of the spectrum.

The role of the eight hopping constants t is just to set an energy scale. Change the hopping constants amounts to stretching the butterfly spectrum vertically, which is an overall scaling to the energy levels. Thus it does not give rise to any interesting physical phenomenon. The three-band spectrum contains a complex and rich physics insight but it seem remains the fractal structure
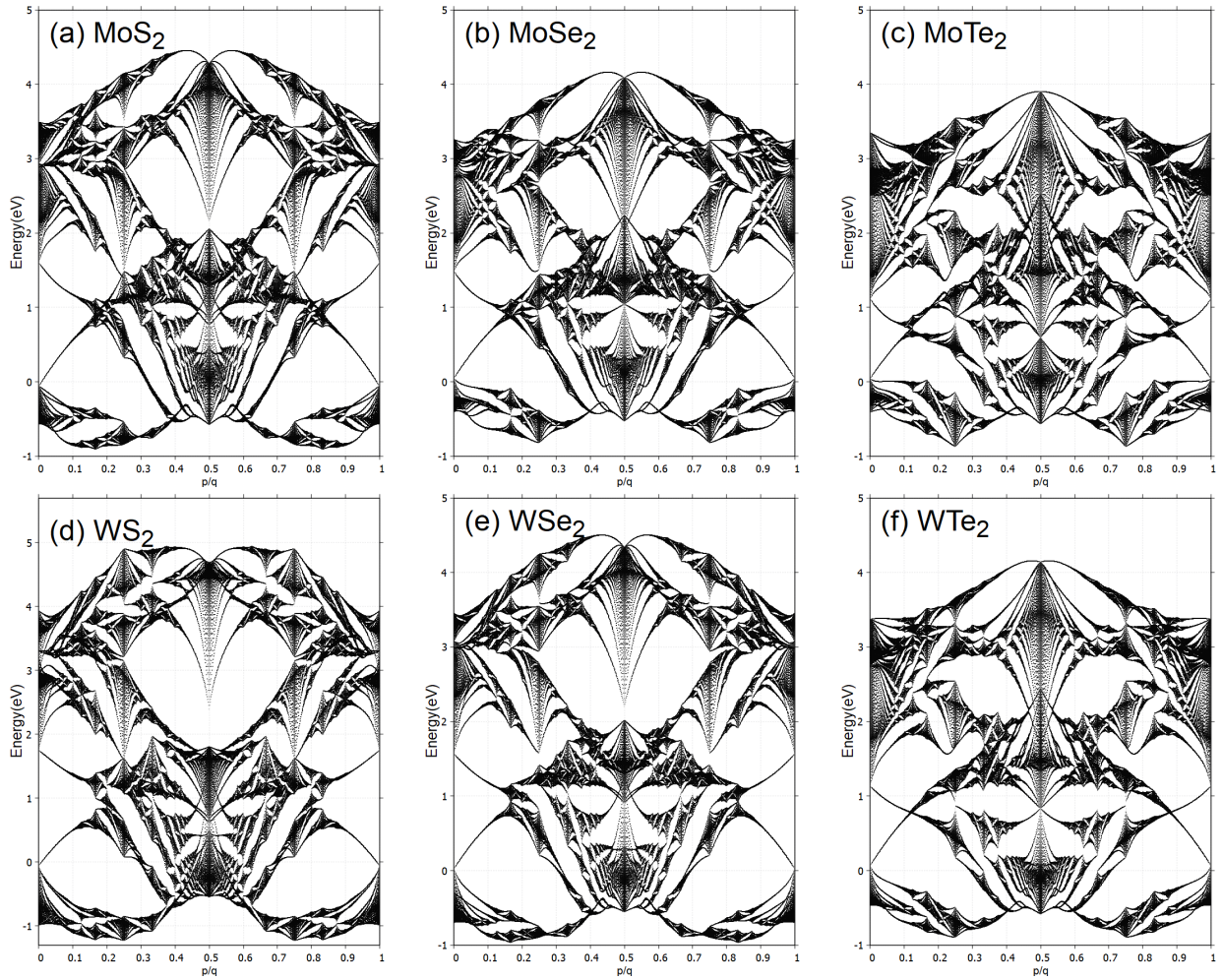
Figure 2.7: Hofstadter's butterflies of MX_2 monolayers using GGA parameters from Table 1.

Due to the significant mass of the transition-metal atom M, its spin orbit coupling (SOC) can be large. For simplicity, we consider only the on-site contribution, which corresponds to the $\mathbf{L} \cdot \mathbf{S}$ term originating from the M atoms. Using the basis set $\left\{ \left| d_{z^2}, \uparrow \right\rangle, \left| d_{xy}, \uparrow \right\rangle, \left| d_{x^2-y^2}, \uparrow \right\rangle, \left| d_{z^2}, \downarrow \right\rangle, \left| d_{xy}, \downarrow \right\rangle, \left| d_{x^2-y^2}, \downarrow \right\rangle \right\}$, we derive the SOC term in the Hamiltonian as

$$H' = \lambda \mathbf{L} \cdot \mathbf{S} = \frac{\lambda}{2} \begin{pmatrix} L_z & L_x - iL_y \\ L_x + iL_y & -L_z \end{pmatrix}, \tag{2.42}$$

in which

$$L_z = \begin{pmatrix} 0 & 0 & 0 \\ 0 & 0 & 2i \\ 0 & -2i & 0 \end{pmatrix}, \tag{2.43}$$

is the matrix of $\hat{L}_z$ (z component of the orbital angular momentum) in bases of $d_{z^2}, d_{xy}, d_{x^2-y^2}$ and λ is characterized the strength of the SOC. Noting that, under the three bases, the

matrix elements of $\hat{L}_x$ and $\hat{L}_y$ are all zeros. Therefore the full TB Hamiltonian for the magnetic unit cell with the SOC as follows

$$
\begin{aligned}
H_{\text{SOC}}(\mathbf{k}) &= \mathbf{I}_2 \otimes H(\mathbf{k}) + \mathbf{I}_q \otimes H' \\
&= \begin{pmatrix} H_{3q \times 3q}(\mathbf{k}) + \frac{\lambda}{2}L_z & 0 \\ 0 & H_{3q \times 3q}(\mathbf{k}) - \frac{\lambda}{2}L_z \end{pmatrix},
\end{aligned} \tag{2.44}
$$

in which $\mathbf{I}_2$ is the 2×2 identity matrix.
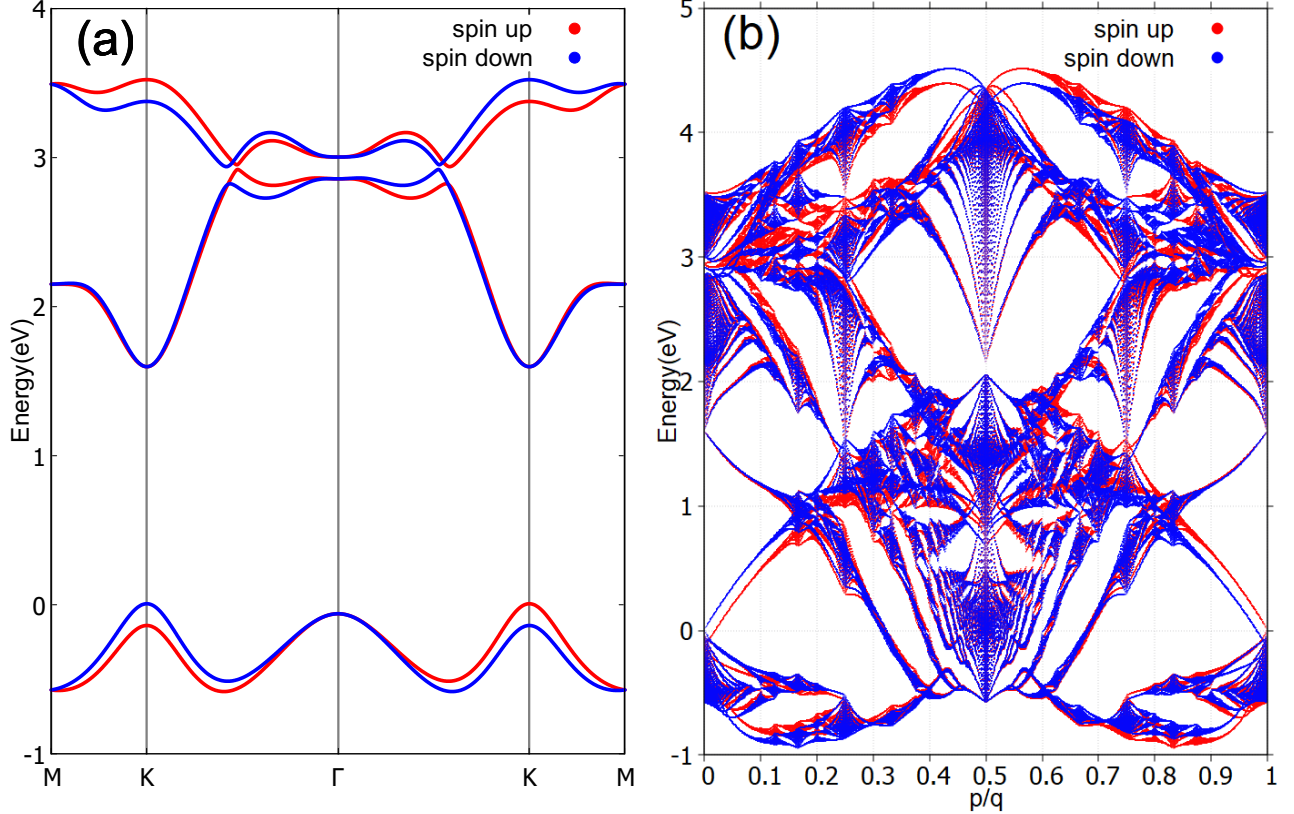
Figure 2.8: Band structure of monolayer MoS_2 along Γ-K direction, SOC causes huge spin splittings in band-structure at K and $-K$ points.

An alternative approach to the derivation of the Hamiltonian under an uniform magnetic field is given in Appendix A.

2.3   Landau levels

In solid-state physics, the behavior of electrons in magnetic fields is usually introduced by using the Hamiltonian

$$
H = \frac{\mathbf{p} + e\mathbf{A}(\mathbf{r})^2}{2m}, \tag{2.45}
$$

and the energy eigenfunctions are known as Landau levels (LLs)

$$E_n = \left(n + 1/2\right)\hbar\omega_c. \tag{2.46}$$

This treatment is for free electrons, but near the bottom of the two-dimensional tight-binding band of TMD we must find a regime in which the electron behaves as a nearly one(At least with a nearly free dispersion relation).

Recalling the result obtained for the dispersion relation of an electron within the TBM

$$h_0 = 2t_0(\cos 2\alpha + 2\cos\alpha\cos\beta) + \epsilon_1, \tag{2.47}$$

The dispersion energy is approximately free-electron-like by Taylor expansion to second order of $\mathbf{k}$

$$
\begin{aligned}
h_0(\mathbf{k}) &\approx 2t_0\left[1 - \frac{a^2k_x^2}{2} + 2\left(1 - \frac{a^2k_x^2}{8}\right)\left(1 - \frac{3a^2k_y^2}{8}\right)\right] \\
&= t_0\frac{3}{16}\left(32 + a^4k_x^2k_y^2\right) - t_0\frac{3}{2}a^2\left(k_x^2 + k_y^2\right) + \epsilon_1,
\end{aligned}
\tag{2.48}
$$

the term a^4 is negligibly small, then we have

$$h_0(\mathbf{k}) \approx 6t_0 - \frac{3}{2}t_0a^2(k_x^2 + k_y^2) + \epsilon_1. \tag{2.49}$$

One of the ways derivation of effective mass m^* is substitution $\hbar\mathbf{k} \to \mathbf{\Pi} + e\mathbf{A}$, with Landau gauge $\mathbf{A} = (0, Bx, 0)$

$$
\begin{aligned}
h_0(\mathbf{\Pi}) &\approx 6t_0 - \frac{3}{2}t_0\frac{a^2}{\hbar^2}\left[\Pi_x^2 + \left(\Pi_y + eBx\right)^2\right] + \epsilon_1 \\
&\approx 6t_0 - \frac{3}{2}t_0\frac{a^2}{\hbar^2}\Pi_x^2 - \frac{3}{2}t_0\frac{a^2}{\hbar^2}(eB)^2\left[x - \left(-\frac{\hbar k_y}{eB}\right)\right]^2 + \epsilon_1.
\end{aligned}
\tag{2.50}
$$

The Eq (2.50) can be rewrite in the form as

$$E(\mathbf{\Pi}) = 6t_0 - \left[\frac{1}{2m^*}\Pi_x^2 + \frac{1}{2}m^*\omega_c^2(x - x_0)^2\right] + \epsilon_1, \tag{2.51}$$

where $m^* = \frac{\hbar^2}{3t_0a^2}$ is the effective mass and $x_0 = \frac{\hbar k_y}{eB}$. Subsequently, the cyclotron frequency is

$$\omega_c = \frac{eB}{m^*} = \frac{8\pi\sqrt{3}t_0}{\hbar}\frac{p}{q}, \tag{2.52}$$

and therefore the Landau levels near the bottom of the band structure can be written

as

$$E_n = 6t_0 - \hbar\omega_c(n + 1/2) + \epsilon_1$$
$$= t_0 \left(6 - 8\pi\sqrt{3}\frac{p}{q}(n + 1/2) \right) + \epsilon_1, \tag{2.53}$$

in linear order of an uniform-flux, where n is Landau index. These levels give rise to what is called "the Landau fan", being very important in the de Haas-van Alphen and Shubnikov-de Haas effects [5] which predicts oscillations of the magnetic moment of a meltal depending on an applied magnetic field.
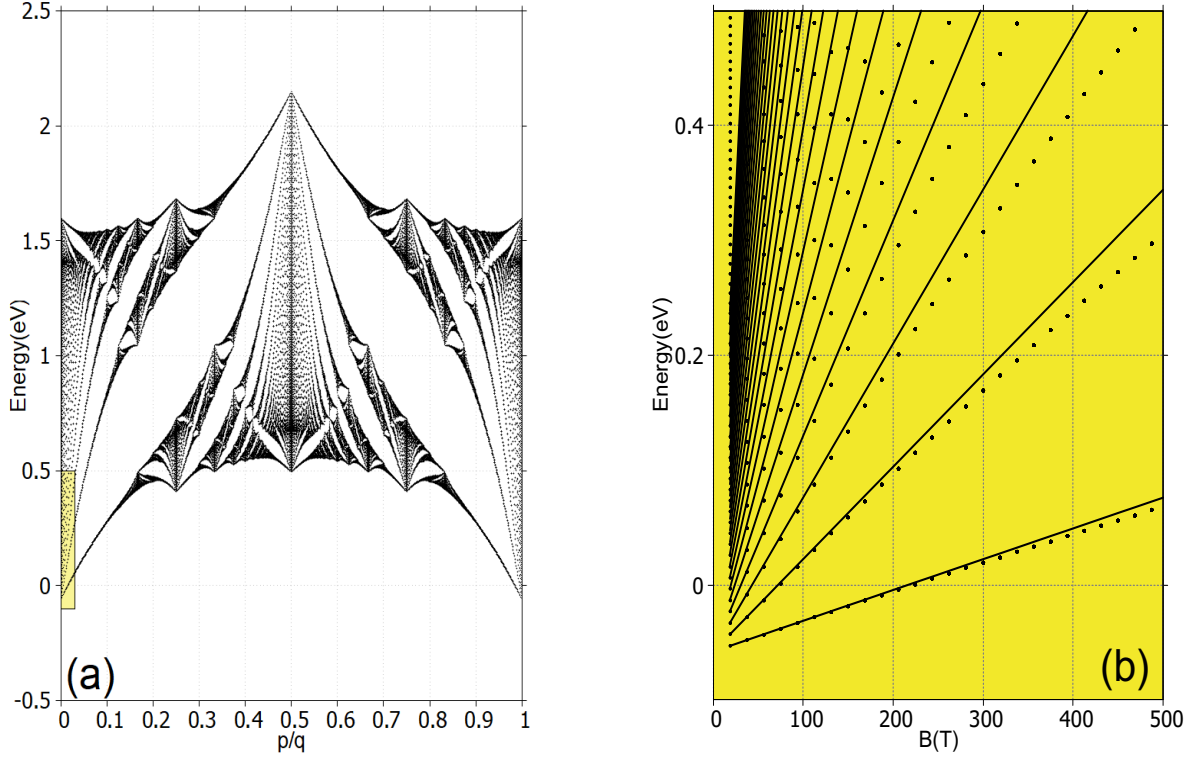

Figure 2.9: (a) Same plot as Fig (2.6) but considering a small area and (b) shows superposition of the Landau fan diagram and the Hofstadter butterfly. Display the first $n = 30$ levels near the bottom of the conduction band for a magnetic field up to $B = 500$ T.

In Fig 2.9 we compare the spectrum of a small section of single-band with $p/q = 1/797$, which is equivalent to small magnetic field, the spectrum of MoS$_2$, with the energy of Landau levels given by Eq.(2.50) show standard equally spaced LLs [6–9] near the bottom of the bands, as plotted in Fig 2.9(b). The fan of LLs can be clearly seen emergin from the partern in Fig 2.9(a).

In Fig 2.9(a), there is just single-band in case zero field, with the effective mass $m^* = \frac{\hbar}{3t_0 a^2}$. The numerical result for this portion of the spectrum are shown in Fig 2.9 for $p/q \geq 1/797$. The first few LLs are clearly seen, and the asymtotic slopes p/q at large q given by Eq. (2.50) are shown for comparison for the first five Landau levels at $B \leq 100$ T. At the values of B the fit is not ideal, but it does seem to be improving

with the decreasing p/q.

Figure 2.9 displays a blowup of the low uniform magnetic region and the LLs as a function of Φ/Φ_0 [10]. The Landau levels are all close to being linear in B, resulting from the magnetic quantization of parabolic bands at $B = 0$ T i.e. increasing values of B, these LLs are sequentially depleted; for $B = 200$ T the levels are completely filled up to the level $n = 4$; for $B = 500$ T it happens the same, only this time are filled up to the level $n = 1$ and so on.

2.4 Hall effects

2.4.1 The classical Hall effect

The Hall effect arises when a conductor carrying an electric current is placed in an external magnetic field $\mathbf{B}$. The Lorentz forece from the magnetic field causes the charges to accumulate on one side of the conductor. Starting with an electric field $\mathbf{E}$ established in the solid results in a current density $\mathbf{J}$ linearly related to the field through Ohm's law

$$\mathbf{J} = \boldsymbol{\sigma}\mathbf{E}, \tag{2.54}$$

$$\mathbf{E} = \sigma^{-1}\mathbf{J} = \rho\mathbf{J}, \tag{2.55}$$

where $\boldsymbol{\sigma}$ is the conductivity tensor and the resistivity ρ is defined as the inverse of the conductivity. This remains true when both are tensors

$$\begin{pmatrix} J_x \\ J_y \end{pmatrix} = \begin{pmatrix} \sigma_{xx} & \sigma_{xy} \\ \sigma_{yx} & \sigma_{yy} \end{pmatrix} \begin{pmatrix} E_x \\ E_y \end{pmatrix}, \tag{2.56}$$

$$\begin{pmatrix} E_x \\ E_y \end{pmatrix} \begin{pmatrix} \rho_{xx} & \rho_{xy} \\ \rho_{yx} & \rho_{yy} \end{pmatrix} \begin{pmatrix} J_x \\ J_y \end{pmatrix}. \tag{2.57}$$

The off-diagonal components of resistivity tensor is $\rho_{xy} = \rho_{yx} = \frac{B}{en}$. Usually we measure the resistance R, which differs from the resistivity ρ by geometric factors. However, for ρ_{xy}, this thing coincide. To see this, consider a sample of material of length L in the y-direction. We drop a voltage V_y in the y-direction and measure the resulting current I_x in the x-direction. The transverse resistance is

$$R_{xy} = \frac{V_y}{I_x} = \frac{LE_y}{LJ_x} = \frac{E_y}{J_x} = -\rho_{xy}. \tag{2.58}$$

For a current I_x flowing in the x-direction, and the corresponded electric field E_y in the y-direction, the Hall coeffcent is defined by

$$R_H = \frac{\rho_{xy}}{B} = \frac{1}{en}. \tag{2.59}$$

showing the Hall resistance is a constant in the classical regime. We see that the Hall coeffcent depends only on microscopic information about the material: the charge and density of conduction particles. The Hall coeffcent does not depend on the scattering time τ; it remains unaffected by the specific frictional mechanism present in the material.
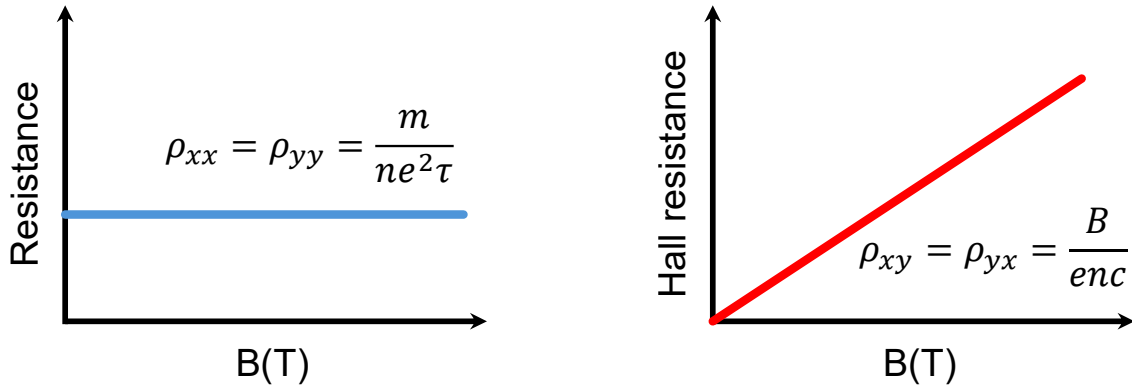

Figure 2.10: The longitudinal resistance on the right figure and the Hall resistance in the left figure. The graph shows both the longitudinal resistance and the Hall resistance is linear to the increasing magnetic field.

2.4.2   The Quantum Hall effect

In previous section, we arrived at the classical Hall resistance, which remains stable under the classical mechanics framework. However, our world is governed not only by classical physics but also by quantum mechanics. Things changes significantly at extremely low temperatures and strong magnetic fields, revaling new quantum phenomena.

There are two related phenomena which are associated to two different quantum Hall effects. These are called the integer Quantum Hall effect (IQHE) and fractional Quantum Hall effect (FQHE). In this study, we mainly focus on the IQHE where the flux number and flux quanta are integers. This phenomenon can be understood without taking into account the Coulomb interaction between electrons, which means we will continue using the single electron Hamiltonian that we described in Section 2. In this section, we first discovered and subsequenly understood theoretically the integer quantum Hall effect in the Hofstadter butterfly.

In two dimensional, there is a crucial relationship between the conductivity tensor

$\boldsymbol{\sigma}$ and the resistivity tensor $\boldsymbol{\rho}$ is given by

$$\begin{bmatrix} \sigma_{xx} & \sigma_{xy} \\ \sigma_{yx} & \sigma_{yy} \end{bmatrix} \begin{bmatrix} \rho_{xx} & \rho_{xy} \\ \rho_{yx} & \rho_{yy} \end{bmatrix}^{-1} = \frac{1}{\rho_{xx}\rho_{yy} - \rho_{xy}\rho_{yx}} \begin{bmatrix} \rho_{yy} & -\rho_{xy} \\ -\rho_{yx} & \rho_{xx} \end{bmatrix}. \qquad (2.60)$$

Let's take a look at the experimental data for the quantum Hall effect were perfomed in 1980 by von Klitzing *et at.* [11]
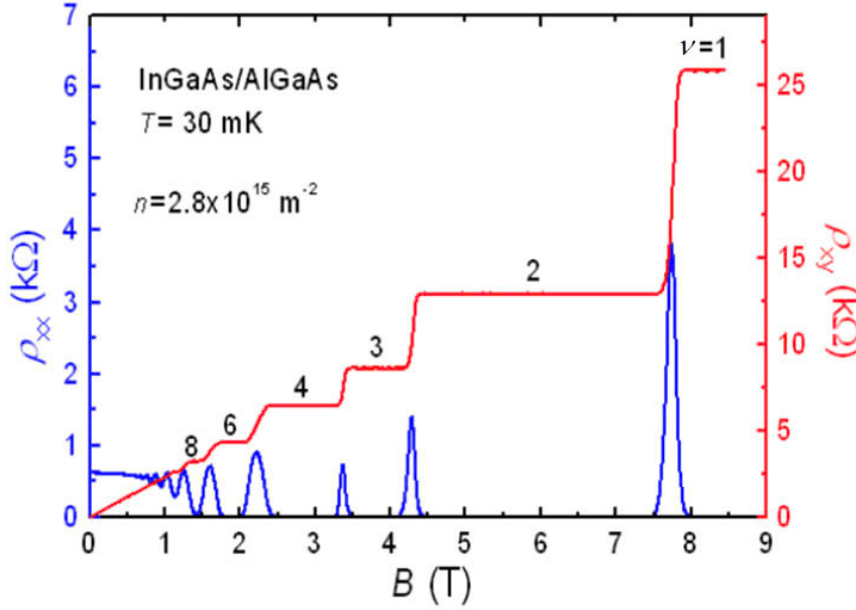

Figure 2.11: This is the integer quantum Hall effect. For this Klaus von Klitzing was awarded the 1985 Nobel prize.

Both the Hall resistivity ρ_{xy} and the longitudinal resistivity ρ_{xx} depict interesting behaviour. Perhaps the most striking feature in the figure is the fact that the Hall resistivity ρ_{xy} sits on a plateau for a range of magnetic field, before jumping dramatically to the next plateau, while the longitudinal spikes sharply at the transistions between plateuax but vanishes on the plateaux themsleves.

The Hall resistivity is now defined

$$\rho_{xy} = \frac{R_K}{\nu}, \quad \nu = 1, 2, \dots \qquad (2.61)$$

while ν is the total filled Landau levels and R_K is Klitzing's resistance constant

$$R_K = \frac{h}{e^2} = 25812.8074555\Omega \pm 0.0000059\Omega. \qquad (2.62)$$

Between two plateaux, if $\rho_{xy} = 0$ then we get the familiar relation between resistivity

and conductivity is $\sigma_{xx} = 1/\rho_{xx}$. But on these Hall plateaux

$$\rho_{xy} = \rho_{yx} = \text{const}, \ \rho_{xx} = \rho_{yy} = 0, \tag{2.63}$$

this leads to

$$\sigma_{xy} = \sigma_{yx} = 1/\text{const}, \ \sigma_{xx} = \sigma_{yy} = 0. \tag{2.64}$$

There is an apparent paradox here, we would call a system with $\rho_{xx} = 0$ is a perfect conductor, while one with $\sigma_{xx} = 0$ is a perfect insulator. But what if both $\rho_{xx} = 0$ and $\sigma_{xx} = 0$ occur simultaneously? A new material or a new state of matter?

2.4.3 Color the Hofstadter butterfly

The contribution to the Hall conductivity from a single subband is given by [12–15]

$$\sigma_{xy} = \frac{e^2}{h} \sum_n^{\text{occ.}} \frac{1}{2\pi} \oiint_{\text{BZ}} dk_x dk_y \Omega_n^z(\mathbf{k}). \tag{2.65}$$

In general, the Berry curvature intergrated over a closed manifold is quantized in the units of e^2/h and equals to the net number of monopoles inside. This number is called the Chern number and is responsible for a number of quantization effects. Therefore the Hall conductivity is quantized for a two dimensional band insulator of noninteracting electrons. Since the integral for the whole Brillouin zone respectively Berry curvature, we arrived at the Thouless-Kohmoto-Nightingale-Nijs (TKNN)'s formula [15]

$$\sigma_{xy} = \frac{e^2}{h}\nu, \quad \nu = 1, 2, ... \tag{2.66}$$

ν is guaranteed to be an integer given by the Chern number.

We, then, calculate the quantum Hall conductivity by the Streda formula [16]

$$\sigma_{xy}(B, E_F) = e\frac{\partial N(E, B)}{\partial B}\bigg|_{E=E_F}, \tag{2.67}$$

where $N(E_F, B)$ is the number of state at fixed Fermi energy E_F. Combining Eq. (2.66) and Eq. (2.67), we have

$$\frac{\partial N}{\partial B} = \frac{e}{h}\nu. \tag{2.68}$$

Assuming that B vary slightly

$$N = c + \frac{e}{h}B\nu, \quad c \text{ is any constant.} \tag{2.69}$$

Before this, we have defined $\frac{p}{q} = \frac{eBa^2\sqrt{3}}{4h}$, with $S = \frac{\sqrt{3}a^2}{4}$ is the area of the original unit cell in Section 2.2. Multiply S with Eq. (2.69), we have

$$N \times S = c + \frac{p}{q}\nu, \tag{2.70}$$

and the density of electron in a single band is given by $\frac{1}{Sq}$, thus when there are r bands below the Fermi energy level, the density of electron for r^{th} band is

$$N = \frac{r}{Sq}. \tag{2.71}$$

Then, the Eq. (2.70), is written as,

$$r = c \times q + p \times \nu_r, \tag{2.72}$$

in this equation r, q, p, ν are integers, thus, $c \times q$ must be an integer. On the one hand, since c is independent of q, and q can change when the magnetic field is varied without making a point of contact, then c itself must be an integer, namely s_r. Thus we have

$$r = q \times s_r + p \times \nu_r, \tag{2.73}$$

this equation is usually named as the Diophantine equation. While ν is the Chern number associated with the quantized Hall conductance, s is another integer that play a role to indentify the gap index.

The Hall conductivity of the lattice model for an electron in a background magnetic field can only be computed when the flux ratio $\frac{\Phi}{\Phi_0} = \frac{p}{q}$ is rational. In this case, we can use the TKNN formula, but with the Chern number, which used to be defined by intergrating over the Brillouin zone, now arising by intergrating over the magnetic Brillouin zone. Others derivation is in [17–19].

The Diophantine equation is crucial in understanding the quantization of Hall conductance in the Hofstadter butterfly. The Chern number ν determines the topological nature of the bands and their contribution to the Hall conductance, while the integer s identifies specific energy gaps in the spectrum. These gaps are directly linked to incompressible quantum Hall states, which are of significant interest in both theoretical and experimental condensed matter physics.

To further explore the intricate fractal nature of the Hofstadter spectrum, we shall now achieve the colored Hofstadter butterfly. There are many ways to color the butterfly. For instance, a common approach is to color each point of the butterfly based on their Chern number, as illustrated in the Fig 2.12. At these points, the Hall conductivity hightlights exactly quantization. However, a drawback of this method is that the butterfly may contain a dense of points, which can make it difficult to visualise fine details in the colored spectrum.
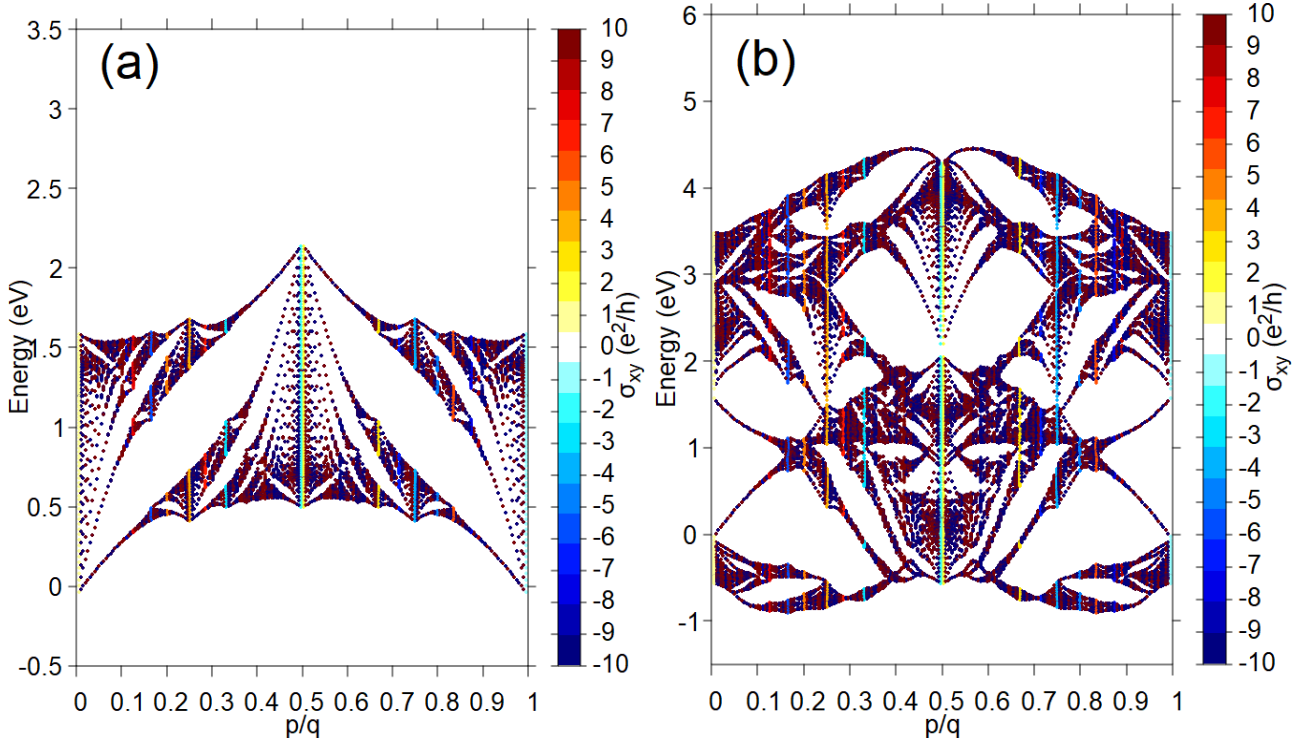

Figure 2.12: q = 199 và q = 797

Fig 2.13 displays the Hofstadter butterfly, color-coded according to the Hall conductance. Moreover, the number p increases simultaneously with Chern number, making it challenging to maintain a fixed scale. Therefore, to address this, we limit the Chern number scale within $-10 \leq \nu \leq 10$, any Chern number outside this range is set to zero. Regions with zero Hall conductance and the corresponding spectrum are left blank. Remarkably, the two largest gaps near the center of the figure are associated with small integers where the color coding accurately reflects their values. Unlike the traditional Hofstadter butterfly, which hightlights the spectrum, this version emphasizes the gaps by using a color scheme to characterize different Hall conductance.
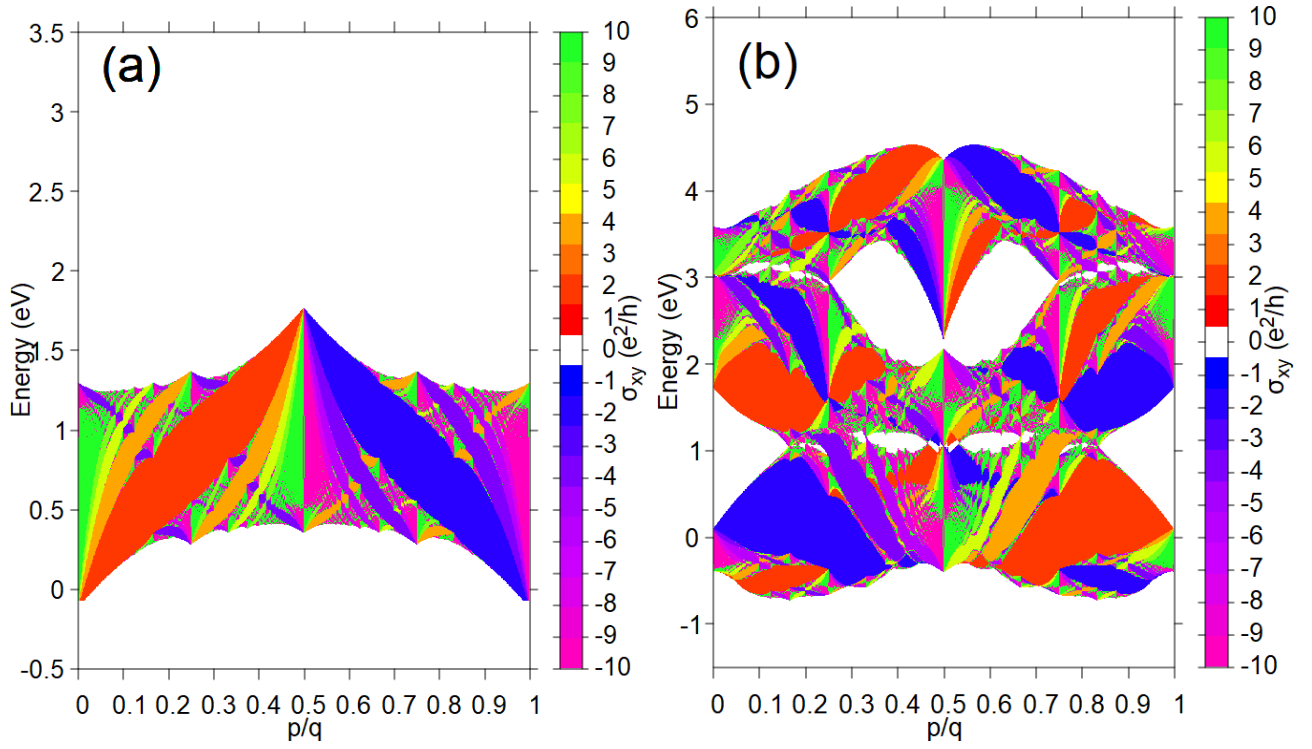
Figure 2.13: q = 199 và q = 797. This color pallete was famously made by Avron[19].

Both figures display rich physics insights, it totally use two different methods to color the butterfly. While Figure 2.12 uses the sum of the Chern numbers of the occupied bands, Figure 2.13 relies only on the Chern numbers that corresponded to the gap index. However, the colored spectrum not only helps visualize the topological properies of the sysem but also both explain that as the magnitude B increases, the number of occupied bands decreases.

Figure 2.14: q = 199 và q = 797. This color pallete was famously made by gnuplot.

CHAPTER 3

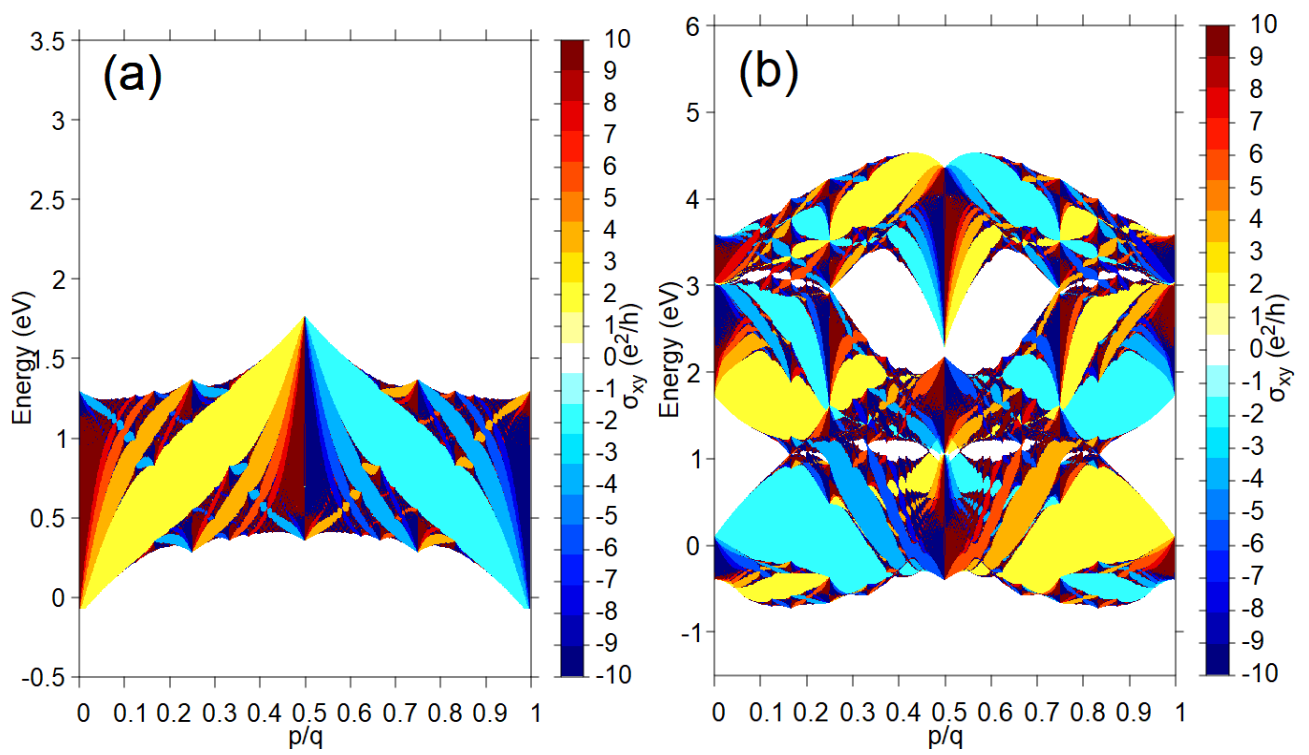# RESULT AND DISCUSSION

CHAPTER 4

CONCLUSION AND FUTURE WORK

4.1 Conclusion

In our research, we have calculated the Hofstadter butterfly of monolayer MoS_2 and others transistion metal dichalcogenide types by using a tight-binding three-band model. In addition, we have explored the rich and complex physics of monolayer MoS_2, such as Landau levels and integer quantum Hall effect (IQHE), in the presence of external magnetic fields. The research conducted within these pages has demonstated the unique interplay between the superlattice and magnetic fields, which leads to the emergence of fascinating quantum phenomena.

In section 2.1, we have studied the tight-binding three-band model for monolayers of MX_2 using only the $M-d_{z^2}$, d_{xy} and $d_{x^2-y^2}$ orbitals. When only NN M-M hoppings are included, we calculated the hopping energies using the symmetry of the D_{3h} point group we derived eights hopping parameters from Ref [1].

In section 2.2, we focused on the Hofstadter physics in monolayer TMD, where the lattice gives rise to a rich Hofstadter spectrum when subjected to a magnetic field. The detailed analysis revealed key features of the spectrum, including the SOC and the emergence of topological quantum Hall states. In addition, the study also demonstrated that there are many ways to derivive the Hofstadter spectrum two of those is using the Peierls substitution or Envelope Function Approximation.

In section 2.3 and section 2.4, extended the investigation into the realm of Hall effects, introducing the Landau levels, the integer quantum Hall effect and applying it to monolayer TMD systems. We also shown that how the Hofstadter butterfly can be colored in various ways using the Chern number.

Overall, while this study provides valuable insights, we acknowledge several limitations. Firstly, in section 2.3, our calculation was restrited to the single-band approx-

imation due to the computational complexity of multi-band interactions. Specifically, incorporating three-band model would require significantly more resources, particularly in calculating Chern numbers, which are numerically intensive for larger Hamiltonian matrices, this significantly cause a time consumption. For example, to achived the colored butterfly, it costs us around two days for a better resolution.

4.2   Future work

For further research, we

APPENDIX A

Details of the Peierls substitution

As we mentioned in Section 2.2, we work in the Landau gauge $\mathbf{A} = (0, Bx, 0)$. The Peierls phase is given as $\theta_{i,i'} = \int_i^{i'} \mathbf{A} \cdot d\mathbf{r}$. By making an parametrization, for instance

$$
\begin{cases}
x = x_m + (x_{m'} - x_m)\tau, \\
y = y_n + (y_{n'} - y_n)\tau,
\end{cases}
\tag{A.1}
$$

where $\tau \in [0, 1]$ and $i = (m, n)$, thanks to the Landau gauge, the path integral resembles to $\int Bx dy$, the phases can be written as

$$
\begin{aligned}
\theta_{i,i'} &= \frac{eB}{\hbar} \int_0^1 \left[x_m + (x_{m'} - x_m)\tau \right] (y_{n'} - y_n) d\tau \\
&= \frac{eB}{\hbar} (x_m + \frac{x_{m'} - x_m}{2})(y_{n'} - y_n) \\
&= \frac{eB}{\hbar} \left(\frac{x_m + x_{m'}}{2} \right) (y_{n'} - y_n).
\end{aligned}
\tag{A.2}
$$

From this, the Peierls phase depends on absolute x coordinates but only relative to y coordinates.

APPENDIX B

Harper's equation

We now consider the case of hexagonal lattice with one band as a basis under an uniform magnetic field given by the Landau gauge $\mathbf{A} = (0, Bx, 0)$. Given

$$
\begin{aligned}
h_0 &= 2t_0 \left(\cos 2\alpha + 2 \cos \alpha \cos \beta \right) + \epsilon_1 \\
&= 2t_0 \left[\cos(k_x a) + 2 \cos \left(\frac{k_x a}{2} \right) \cos \left(\frac{\sqrt{3} k_y a}{2} \right) \right] + \epsilon_1 \\
&= 2t_0 \left\{ \cos(k_x a) + \cos \left[\left(k_x + \sqrt{3} k_y \right) \frac{a}{2} \right] + \cos \left[\left(k_x - \sqrt{3} k_y \right) \frac{a}{2} \right] \right\} + \epsilon_1 \\
&= 2t_0 \left\{ \cos \left(\Pi_x \frac{a}{\hbar} \right) + \cos \left[\left(\Pi_x + \sqrt{3} eBx + \sqrt{3} \Pi_y \right) \frac{a}{2\hbar} \right] \right. \\
&\quad \left. + \cos \left[\left(\Pi_x - \sqrt{3} eBx - \sqrt{3} \Pi_y \right) \frac{a}{2\hbar} \right] \right\} + \epsilon_1 \\
&= t_0 \left[e^{i\Pi_x \frac{a}{\hbar}} + e^{-i\Pi_x \frac{a}{\hbar}} + e^{i(\Pi_x + \sqrt{3} eBx + \sqrt{3} \Pi_y)a/2\hbar} + e^{-i(\Pi_x + \sqrt{3} eBx + \sqrt{3} \Pi_y)a/2\hbar} \right. \\
&\quad \left. + e^{i(\Pi_x - \sqrt{3} eBx - \sqrt{3} \Pi_y)a/2\hbar} + e^{-i(\Pi_x - \sqrt{3} eBx - \sqrt{3} \Pi_y)a/2\hbar} \right] + \epsilon_1 .
\end{aligned}
\tag{B.1}
$$

We replaced $\hbar\mathbf{k}$ in the above function by the operators $\mathbf{\Pi} + e\mathbf{A}/c$ in order to create an operator out of h_0. However, the quantity $\hbar\mathbf{k}$ is represents the crystal momentum, it is more precise interpretation is to regard $\mathbf{k}$ as a quantum number which describes a Bloch state. This method can be achived by using Envelope Function Approximation (EFA). However, we must be very careful regarding how the operators act on the wave functions, since $[x, \Pi_x] \neq 0$. In their article, Gumbs and Fekete [21] incorrectly applied the modified translation operators, leading to completely incorrect results. In this work, we treat the operators more correctly by applying the Baker-Campbell-Hausdorff (BCH) formula and

taking into account the commutation relation $[x, \Pi_x] = i\hbar$

$$
\begin{aligned}
e^{\pm i(\Pi_x + \sqrt{3}eBx)a/2\hbar} &= e^{\pm i\Pi_x a/2\hbar} e^{\pm i\sqrt{3}eBxa/2\hbar} e^{-\frac{1}{2}\left[\pm i\Pi_x, \pm i\sqrt{3}eBx\right]a^2/2\hbar^2} \\
&= e^{\pm i\Pi_x a/2\hbar} e^{\pm i\sqrt{3}eBxa/2\hbar} e^{\mp i\sqrt{3}eBa^2/8\hbar}.
\end{aligned}
\tag{B.2}
$$

Substituting $x = \dfrac{ma}{2}$ into (B.2), this leads to

$$
e^{\pm i(\Pi_x + \sqrt{3}eBx)a/2\hbar} = e^{\pm i\Pi_x a/2\hbar} e^{\pm i\sqrt{3}eB(m+1/2)a^2/4\hbar}.
\tag{B.3}
$$

And

$$
\begin{aligned}
e^{\pm i(\Pi_x - \sqrt{3}eBx)a/2\hbar} &= e^{\pm i\Pi_x a/2\hbar} e^{\mp i\sqrt{3}eBxa/2\hbar} e^{-\frac{1}{2}\left[\pm i\Pi_x, \mp i\sqrt{3}eBx\right]a^2/2\hbar^2} \\
&= e^{\pm i\Pi_x a/2\hbar} e^{\mp i\sqrt{3}eBxa/2\hbar} e^{\mp i\sqrt{3}eBa^2/8\hbar},
\end{aligned}
\tag{B.4}
$$

substituting $x = \dfrac{ma}{2}$ into (B.4), this leads to

$$
e^{\pm i(\Pi_x - \sqrt{3}eBx)a/2\hbar} = e^{\pm i\Pi_x a/2\hbar} e^{\mp i\sqrt{3}eB(m-1/2)a^2/4\hbar}.
\tag{B.5}
$$

The operators $e^{\pm i\Pi_x a/2\hbar}$, $e^{\pm i\Pi_y \sqrt{3}a/2\hbar}$ can be regconized as translational operators, we can rewrite (B.3) as

$$
\begin{aligned}
&t_0\varphi_0(x+a, y) + t_0\varphi_0(x-a, y) + t_0\varphi_0(x+\frac{a}{2}, y+\frac{a\sqrt{3}}{2}) e^{\frac{ie}{\hbar}B(m+1/2)\frac{a^2\sqrt{3}}{4}} \\
&+t_0\varphi_0(x+\frac{a}{2}, y-\frac{a\sqrt{3}}{2}) e^{-\frac{ie}{\hbar}B(m+1/2)\frac{a^2\sqrt{3}}{4}} + t_0\varphi_0(x-\frac{a}{2}, y+\frac{a\sqrt{3}}{2}) e^{\frac{ie}{\hbar}B(m+1/2)\frac{a^2\sqrt{3}}{4}} \\
&+t_0\varphi_0(x-\frac{a}{2}, y-\frac{a\sqrt{3}}{2}) e^{-\frac{ie}{\hbar}B(m-1/2)\frac{a^2\sqrt{3}}{4}} + \epsilon_1\varphi_0(x,y) = E_1\varphi_0(x,y),
\end{aligned}
\tag{B.6}
$$

for the sake of simplicity we have defined $\varphi_0 \equiv |d_{z^2}\rangle$.

It is reasonable to assume planewave behavior in the y direction, since the coefficents in the above equation only involve x. Therefore, we can assume the partial solution for y to be in the form

$$
\varphi(\frac{ma}{2}, \frac{na\sqrt{3}}{2}) = e^{ik_y n\frac{a\sqrt{3}}{2}} \varphi(m),
\tag{B.7}
$$

which reduces (B.6) to

$$
\begin{aligned}
&t_0\varphi_0(m+2) + t_0\varphi_0(m-2) + t_0\varphi_0(m+1) e^{2i\pi(m+1/2)p/q} e^{ik_y a\sqrt{3}/2} \\
&+t_0\varphi_0(m+1) e^{-2i\pi(m+1/2)p/q} e^{-ik_y a\sqrt{3}/2} + t_0\varphi_0(m-1) e^{2i\pi(m-1/2)p/q} e^{ik_y a\sqrt{3}/2} \\
&+t_0\varphi_0(m-1) e^{-2i\pi(m-1/2)p/q} e^{-ik_y a\sqrt{3}/2} + \epsilon_1\varphi_0(m) = E_1\varphi_0(m),
\end{aligned}
\tag{B.8}
$$

this is equivalent to Eq. 2.16 we have mentioned in Section 2.2. Equation B.8 is sometimes called "Harper's equation"[3, 22] Since different m values give different equations, one reaches a unique set of equations when Φ/Φ_0 is a rational number p/q and m goes through q different values, essentially resulting in the Hamiltonian matrix written for a magnetic unit cell enlarged in x direction q times.

In the case of TMD presented in [1], the contribution of the X atom has been neglected, leading to the transformation of the hexagonal crystal structure of TMD into a regular triangular lattice. From there, we can map the triangular lattice to the case of the square lattice. In the triangular lattice, it has been established that the translation operators must satisfy the Baker-Campbell-Hausdorff formula.

APPENDIX C

Solving the Diophantine equation

We have defined that the magnetic flux through a unit cell is $\frac{\Phi}{\Phi_0} = \frac{p}{q}$. For p and q are mutually prime numbers, we defined the pairs $(\nu_r, s_r) = (m, n)$ as the solutions for Diophantine equation

$$pm + qn = \gcd(p, q). \tag{C.1}$$

Fortunately, p and q are co-prime, (B.1) is now

$$pm + qn = 1, \tag{C.2}$$

By deviding p by q, we get a quotient a and a remainder b. They satisfy

$$q = pa + b. \tag{C.3}$$

By using the Euclidean Algorithm, we can easily find (m, n). For instance, the rational magnetic flux is $\frac{p}{q} = \frac{30}{47}$, then the diophantine equation now is $30m + 47n = 1$, and

$$
\begin{aligned}
47 &= 30 \times 1 + 17, \\
30 &= 17 \times 1 + 13, \\
17 &= 13 \times 1 + 4, \\
13 &= 4 \times 3 + 1.
\end{aligned}
\tag{C.4}
$$

At this point we stop, because we arrived at the greatest common divisor, so the algorithm is over. The next step is solve for the remainders

$$
\begin{aligned}
47 &= 30 \times 1 + 17 \Rightarrow 17 = 47 \times 1 + 30 \times (-1), \\
30 &= 17 \times 1 + 13 \Rightarrow 13 = 30 \times 1 + 17 \times (-1), \\
17 &= 13 \times 1 + 4 \Rightarrow 4 = 17 \times 1 + 13 \times (-1), \\
13 &= 4 \times 3 + 1 \Rightarrow 1 = 13 \times 1 + 4 \times (-3).
\end{aligned}
\tag{C.5}
$$

We are going to take this last remainder equation, and do backwards substitute until we get the very first remainder

$$
\begin{aligned}
1 &= 13 \times 1 + 4 \times (-3) \\
&= 13 \times 1 + [17 \times 1 + 13 \times (-1)] \times (-3) \\
&= 13 \times 4 + 17 \times (-3) \\
&= [30 \times 1 + 17 \times (-1)] \times 4 + 17 \times (-3) \\
&= 30 \times 4 + 17 \times (-7) \\
&= 30 \times 4 + [47 \times 1 + 30 \times (-1)] \times (-7) \\
&= 30 \times (11) + 47 \times (-7),
\end{aligned}
\tag{C.6}
$$

we find the solution for (m, n) is $(11, -7)$.

REFERENCES

[1] Gui-Bin Liu, Wen-Yu Shan, Yugui Yao, Wang Yao, and Di Xiao. Three-band tight-binding model for monolayers of group-vib transition metal dichalcogenides. *Phys. Rev. B*, 88:085433, Aug 2013.

[2] Fırat Yalçın. Tight binding investigation of graphene nanostructures under magnetic field. Master's thesis, Middle East Technical University, 2019.

[3] Douglas R. Hofstadter. Energy levels and wave functions of bloch electrons in rational and irrational magnetic fields. *Phys. Rev. B*, 14:2239–2249, Sep 1976.

[4] Yakir Aharonov and David Bohm. Significance of electromagnetic potentials in the quantum theory. *Physical review*, 115(3):485–497, 1959.

[5] James G. Analytis, Stephen J. Blundell, and Arzhang Ardavan. Landau levels, molecular orbitals, and the hofstadter butterfly in finite systems. *American Journal of Physics*, 72(5):613–618, 05 2004.

[6] D. Shoenberg. *Magnetic Oscillations in Metals*. Cambridge Monographs on Physics. Cambridge University Press, 1984.

[7] J. Singleton. *Band Theory and Electronic Properties of Solids*. Oxford Master Series in Condensed Matter Physics. OUP Oxford, 2001.

[8] S. Blundell. *Magnetism in Condensed Matter*. Oxford Master Series in Condensed Matter Physics 4. OUP Oxford, 2001.

[9] C. Kittel. *Quantum Theory of Solids*. Wiley, 1987.

[10] Juan Li, Yi-Fei Wang, and Chang-De Gong. Tight-binding electrons on triangular and kagomé lattices under staggered modulated magnetic fields: quantum hall effects and hofstadter butterflies. *Journal of Physics: Condensed Matter*, 23(15):156002, apr 2011.

[11] K. v. Klitzing, G. Dorda, and M. Pepper. New method for high-accuracy determination of the fine-structure constant based on quantized hall resistance. *Phys. Rev. Lett.*, 45:494–497, Aug 1980.

[12] Mahito Kohmoto. Zero modes and the quantized hall conductance of the two-dimensional lattice in a magnetic field. *Physical Review B*, 39(16):11943, 1989.

[13] Yasuhiro Hatsugai and Mahito Kohmoto. Energy spectrum and the quantum hall effect on the square lattice with next-nearest-neighbor hopping. *Physical review B*, 42(13):8282, 1990.

[14] Mahito Kohmoto. Topological invariant and the quantization of the hall conductance. *Annals of Physics*, 160(2):343–354, 1985.

[15] D. J. Thouless, M. Kohmoto, M. P. Nightingale, and M. den Nijs. Quantized hall conductance in a two-dimensional periodic potential. *Phys. Rev. Lett.*, 49:405–408, Aug 1982.

[16] P Streda. Theory of quantised hall conductivity in two dimensions. *Journal of Physics C: Solid State Physics*, 15(22):L717, 1982.

[17] Francesco Di Colandrea, Alessio d'Errico, Maria Maffei, Hannah M Price, Maciej Lewenstein, Lorenzo Marrucci, Filippo Cardano, Alexandre Dauphin, and Pietro Massignan. Linking topological features of the hofstadter model to optical diffraction figures. *New Journal of Physics*, 24(1):013028, 2022.

[18] Itzhack Dana, Yosi Avron, and J Zak. Quantised hall conductance in a perfect crystal. *Journal of Physics C: Solid State Physics*, 18(22):L679, 1985.

[19] Joseph E Avron, Daniel Osadchy, and Ruedi Seiler. A topological look at the quantum hall effect. *Physics today*, 56(8):38–42, 2003.

[20] GH Wannier. A result not dependent on rationality for bloch electrons in a magnetic field. *physica status solidi (b)*, 88(2):757–765, 1978.

[21] Godfrey Gumbs and Paula Fekete. Hofstadter butterfly for the hexagonal lattice. *Phys. Rev. B*, 56:3787–3791, Aug 1997.

[22] Philip George Harper. The general motion of conduction electrons in a uniform magnetic field, with application to the diamagnetism of metals. *Proceedings of the Physical Society. Section A*, 68(10):879–892, 1955.

[23] Andor Kormányos, Viktor Zólyomi, Neil D. Drummond, Péter Rakyta, Guido Burkard, and Vladimir I. Fal'ko. Monolayer mos_2: Trigonal warping, the Γ valley, and spin-orbit coupling effects. *Phys. Rev. B*, 88:045416, Jul 2013.

[24] Branimir Radisavljevic, Aleksandra Radenovic, Jacopo Brivio, Valentina Giacometti, and Andras Kis. Single-layer mos2 transistors. *Nature nanotechnology*, 6(3):147–150, 2011.

[25] Fengyuan Xuan and Su Ying Quek. Valley zeeman effect and landau levels in two-dimensional transition metal dichalcogenides. *Phys. Rev. Res.*, 2:033256, Aug 2020.

[26] Jun John Sakurai and Jim Napolitano. *Modern quantum mechanics*. Cambridge University Press, 2020.

[27] Rudolph Peierls. Zur theorie des diamagnetismus von leitungselektronen. *Zeitschrift für Physik*, 80(11):763–791, 1933.

[28] Gi-Yeong Oh. Energy spectrum of a triangular lattice in a uniform magnetic field: Effect of next-nearest-neighbor hopping. *Journal of the Korean Physical Society*, 37(5):534–539, 2000.

[29] Jenö Sólyom. *Fundamentals of the Physics of Solids: Volume II: Electronic Properties*, volume 2. Springer Science & Business Media, 2008.

[30] David J Griffiths and Darrell F Schroeter. *Introduction to quantum mechanics*. Cambridge university press, 2018.

[31] Di Xiao, Ming-Che Chang, and Qian Niu. Berry phase effects on electronic properties. *Reviews of modern physics*, 82(3):1959–2007, 2010.